

AD-A220 898

NEW DISCHARGE PUMPING METHOD FOR CO₂ LASERS

Sponsored by

Defense Advanced Research Projects Agency (DoD)
Defense Small Business Innovation Research Program

REPORTING DATES:

February 1, 1989 to November 30, 1989

ARPA order No 6259

Issued by U.S. Army Missile Command Under
Contract # DAAH01-88-C-0138

Contract Dates: February 10, 1988 - January 31, 1990

Principal Investigator

Jonah Jacob

Science Research Laboratory, Inc.
15 Ward Street
Somerville, MA 02143
(617)-547-1122

APPROVED FOR PUBLICATION
DISTRIBUTION

"The views and conclusions contained in this document are those of the authors and should not be interpreted as representing the official policies, either expressed or implied, of the Defense Advanced Research Projects Agency or the U.S. Government."

*Original contains color
plates: All DTIC reproductions
will be in black and
white*

90 04 28 080

90 000654

2

DTIC
ELECTE
APR 24 1990
B D

NEW DISCHARGE PUMPING METHOD FOR CO₂ LASERS

Sponsored by

Defense Advanced Research Projects Agency (DoD)
Defense Small Business Innovation Research Program

REPORTING DATES:

February 1, 1989 to November 30, 1989

ARPA order No 6259

Issued by U.S. Army Missile Command Under
Contract # DAAH01-88-C-0138

Contract Dates: February 10, 1988 - January 31, 1990

Principal Investigator

Jonah Jacob

Science Research Laboratory, Inc.
15 Ward Street
Somerville, MA 02143
(617)-547-1122

"The views and conclusions contained in this document are those of the authors and should not be interpreted as representing the official policies, either expressed or implied, of the Defense Advanced Research Projects Agency or the U.S. Government."

~~90 01 16 078~~

TABLE OF CONTENTS

<u>Section</u>		<u>Page</u>
1.0	RESULTS FROM THE SRL CO ₂ LASER	1-1
1.1	Laser Design	1-1
1.2	Pulsed CO ₂ Laser Driver	1-4
1.3	Diagnostics and Data System	1-4
1.4	Discharge Characteristics	1-7
1.5	Laser Performance Results	1-10
2.0	LASER DISCHARGE STABILIZATION	2-1
2.1	Introduction	2-1
2.2	The Steady State Solution	2-2
2.3	Numerical Example	2-7
2.4	Stability Conclusions	2-16
2.5	Numerical Simulations of The Two Dimensional Code	2-17
	2.5.1 A Stiff Current Case	2-19
	2.5.2 Stiff Voltage Source	2-23
3.0	STEADY-STATE CONDUCTION COOLING	3-1
3.1	Conduction Equations	3-1
3.2	Thermal Effect of Pulsed Nature of Heating	3-4
3.3	Scaling of Conduction-Cooled Laser	3-5
3.4	Impact of Conduction Cooling on Beam Quality and Spectral Width in the Steady State	3-7
4.0	ELECTRICALLY GENERATED DENSITY DISTURBANCES	4-1
4.1	Density Response to Nonuniform Pumping	4-1
4.2	Beam Quality	4-4
4.3	Frequency Noise	4-10
4.4	Mode-Medium Instability	4-10
4.5	Persistent Acoustic Disturbances	4-10

Accession For	
NTIS GRA&I	<input checked="" type="checkbox"/>
DTIC TAB	<input type="checkbox"/>
Unannounced	<input type="checkbox"/>
Justification	
By _____	
Distribution/	
Availability Codes	
Dist	Avail and/or Special
A-1	

LIST OF ILLUSTRATIONS

<u>Figure</u>	<u>Page</u>
1.1 Assembly drawing of conduction cooled CO ₂ laser head	1-2
1.2 a) Original and modified electrode profiles b) Schematic of preionization pins embedded in cathode	1-3
1.3 Photograph of COLD-I Pulsed Power Module	1-5
1.4 High voltage probe employing LED's and fiber optics	1-6
1.5 Voltage and current traces from 20 Torr discharge	1-8
1.6 Voltage and current traces from 35 Torr discharge, including current predicted by numerical simulation.	1-9
1.7 Open shutter photograph of 20 Torr discharge	1-11
1.8 Laser output pulse from 20 Torr 3:2:1 (He/N ₂ /CO ₂) discharge a) Observed b) Numerical simulation	1-12
1.9 Laser output pulse from 35 Torr 3:2:1 (He/N ₂ /CO ₂) discharge a) Observed b) Numerical simulation	1-13
2.1 General circuit model	2-3
2.2 Graphical solution for the electric field in the discharge under stiff current condition (I_0 is given).	2-6
2.3 Graphical solution for the electric field E_0 in the discharge under finite impedance conditions. The straight lines describe the function $(V_0 - LE_0)/R$ for different values of the external impedance R	2-8
2.4 The dependence of F/S on the electric field in a 1 atm, CO ₂ laser discharge mixture. The operating field ($E_0 = 8.45$ kV/cm found graphically for the case: $V_0 = 9$ kV/cm, $RS = 400 \Omega\text{cm}^2$, $L = 1$ cm, $\tau = 1 \mu\text{sec}$, and $\beta_0 = 10^5 \text{ sec}^{-1}$. The straight line tangent to the curve F/S allows to determine the impedance ($R_a S = 520 \Omega\text{cm}^2$).	2-9
2.5 The time evolution of the electron and metastable densities in a stiff voltage discharge. The initial electron density ($n_e(O) = 5 \times 10^{11} \text{ cm}^{-3}$) is lower than the steady state density ($n_{eo} = 1.07 \times 10^{12} \text{ cm}^{-3}$) at the given voltage ($V_0 = 8.45$ kV).	2-10

LIST OF ILLUSTRATIONS CONTINUED

<u>Figure</u>		<u>Page</u>
2.6	The time evolution of the electron and metastable densities in a stiff voltage discharge with attachment. Initial electron density ($2 \times 10^{12} \text{ cm}^{-3}$) is higher than the steady state density ($n_{eo} = 1.07 \times 10^{12} \text{ cm}^{-3}$) at the given voltage ($V_O = 8.45 \text{ kV}$).	2-11
2.7	Curves of n_e and E for a volumetrically stable discharge. The parameters are: $n_e(O) = 10^{12} \text{ cm}^{-3}$, $V_O = 9 \text{ kV/cm}$, $RS = 400 \Omega \text{ cm}^2$, $L = 1 \text{ cm}$, $\tau = 1 \mu\text{sec}$, $\beta = 10^5 \text{ sec}^{-1}$.	2-13
2.8	Curves of n_e and E for a low external impedance discharge ($RS = 1 \text{ W cm}^2$). The parameters are $n_e(O) = 10^{12} \text{ cm}^{-3}$, $V_O = 9 \text{ kV/cm}$, $L = 1 \text{ cm}$, $t = 1 \mu\text{sec}$ and $\beta = 10^5 \text{ sec}^{-1}$. The discharge is unstable during the initial evolution phase ($t < 15 \mu\text{sec}$).	2-14
2.9	The curves of n_e and E for a discharge with an above-critical impedance ($RS = 800 \Omega \text{ cm}^2$). All other parameters are the same as in Figs. 3.10 and 3.11. No steady state exists for $RS > R_a S = 520 \Omega \text{ cm}^2$ and the discharge is quenched.	2-15
2.10	Schematic of discharge geometry	2-20
2.11	Plot showing the spatial and temporal variation of the electron density n_e . Curve 1 is the initial spatial variation of n_e at $t=0$. Curve 2 is the spatial variation of n_e at $t=5 \mu\text{s}$, etc. The power supply is assumed to be a stiff current source	2-21
2.12	The curve labeled 1 is the same as the curve labeled 10 in Figure 2.11. This figure shows the spatial variation of n_e every $10 \mu\text{s}$.	2-22
2.13	Same as Figures 2.11 and 2.12 except that power supply is assumed to be a stiff voltage source and the spatial variation of n_e is shown every $3 \mu\text{s}$	2-24
2.14	Same as Figure 2.13 except that n_e was initialized at 10^{10} cm^{-3}	2-25
3.1	Schematic of conduction-cooled CO_2 laser head	3-2
3.2	Temperature rise versus power loading for various channel widths	3-6
3.3	Maximum channel width versus PRF for various steady-state temperature rises	3-8
4.1	Geometry of laser	4-2
4.2	Acoustic response versus normalized pulswidth	4-5

ABSTRACT

SRL has designed, fabricated, and successfully tested a pulsed CO₂ laser system. Laser pulses have been generated with measured output energy of 600 mJ, pulse length 40 μ sec, and conversion efficiency of 14% in a 3:2:1 (He:N₂:CO₂) gas mixture. The laser operates at a total gas pressure between 5 and 40 Torr, and utilizes the COLD-I all-solid-state CO₂ laser driver developed by SRL. Typical current, voltage, and laser output traces are presented and compared to numerically simulated curves, showing reasonable agreement.

The theoretical model of CO₂ laser discharges developed by SRL has been extended and utilized to analyze the steady state solutions and stability criteria for three regimes of operation: the stiff voltage case, the stiff current case, and the finite external impedance case. Numerical solutions are presented for the temporal evolution of the electron (plasma) density, the metastable density, and the electric field under various conditions. The theory of RF discharge stabilization has been extended to two spatial dimensions, and numerical results are presented for the stiff current and the stiff voltage cases.

In a repetitively pulse CO₂ laser, the lasing gas must be cooled between pulses to preserve efficiency. Conduction cooling has been examined by SRL as an advanced alternative to the traditional flow loop approach. This concept minimizes the weight of the laser head. A thermal analysis of a pulsed CO₂ laser head with conduction cooling is presented, along with a discussion of beam quality effects due to acoustic and thermal processes.

SECTION 1

1.0 RESULTS FROM THE SRL CO₂ LASER

During the period of this report, SRL has completed the design, fabrication, and initial testing of a 1 meter conduction cooled CO₂ laser head. In this section, the laser head and the all-solid-state CO₂ laser driver are described, and performance results are compared to numerical simulations.

1.1 Laser Design

An assembly drawing of the CO₂ laser head is shown in Fig. 1.1. The discharge volume is 1 meter long, and the anode-cathode gap is 13.5 cm. The discharge width is limited to 2.0 cm by glass side walls within the laser head. This spacing is designed to enable the removal of heat from the laser gas under repetitively pulsed operation by conduction cooling, as discussed in Section 3. Our calculations predict that operating the laser at a 10 pps repetition rate will result in a steady state temperature rise of 75°C, which will not degrade the laser operation.

The discharge electrodes have smoothly tapered edges along the sides and at the ends to prevent discharge instabilities and arcing. Embedded within the cathode (but electrically isolated) are numerous preionization sites consisting of short wire pins to which a prepulse is applied in order to uniformly initiate the discharge. To date, the laser has been operated with 22 such preionization sites. Typical discharges in 10-40 Torr of the He or He/N₂/CO₂ gas mixtures show an expanding discharge emanating uniformly from the immediate region of the wire pins towards the anode.

The electrode profile is a modified contour designed to eliminate arcing problems originally seen near the electrode edges. The modified profile yields a stable discharge. Both contours are shown in Fig. 1.2, along with a schematic of the preionization pins. Each preionization pin is individually ballasted and then connected to one common capacitor. It has been demonstrated that all the pins fire simultaneously, as long as the ballast resistors exceed 20 Ohms.

In addition to the laser itself, the system includes the pulsed power supply, a gas handling system including a mixing tank, and a CAMAC data acquisition system. These systems were

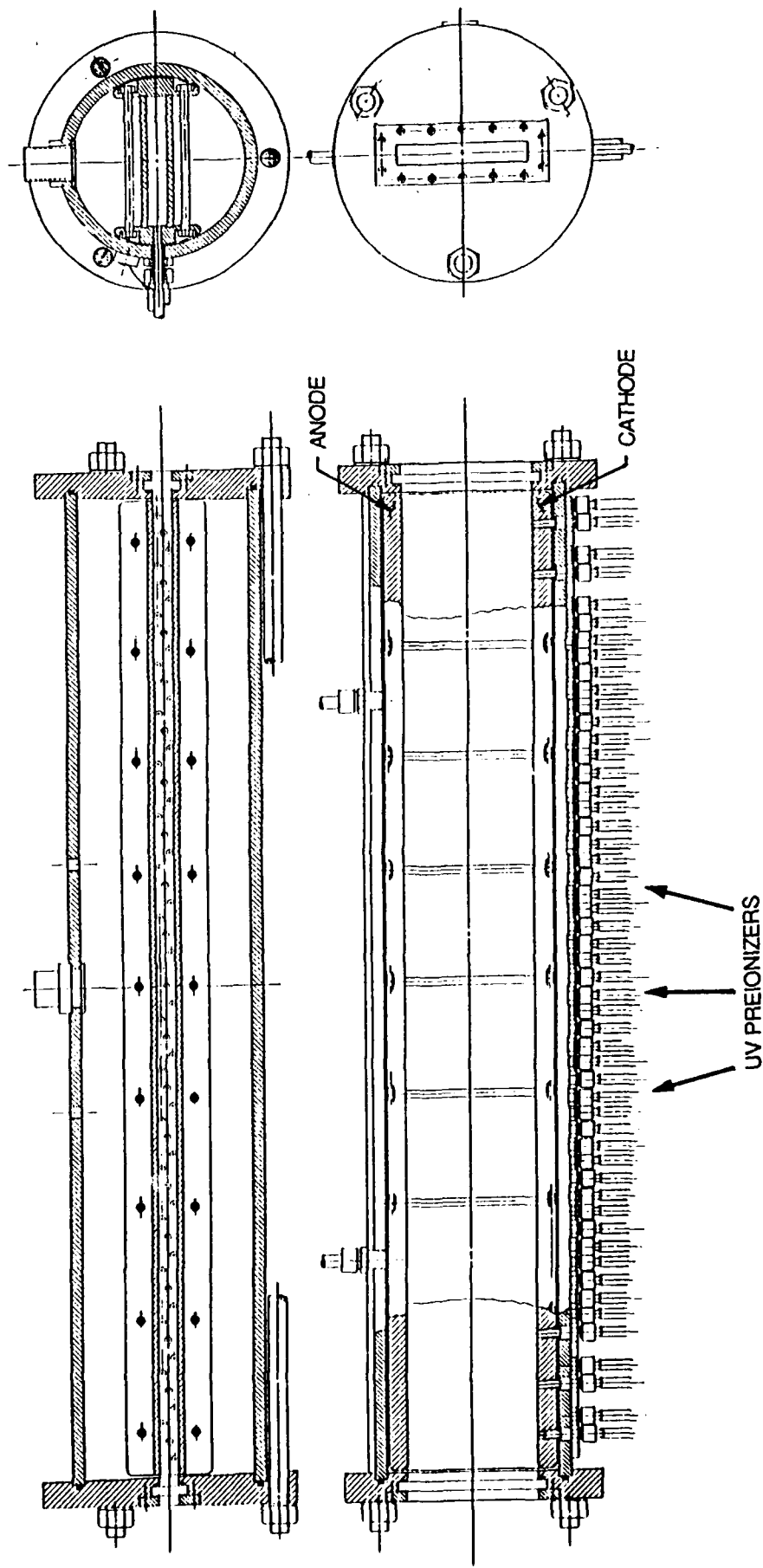
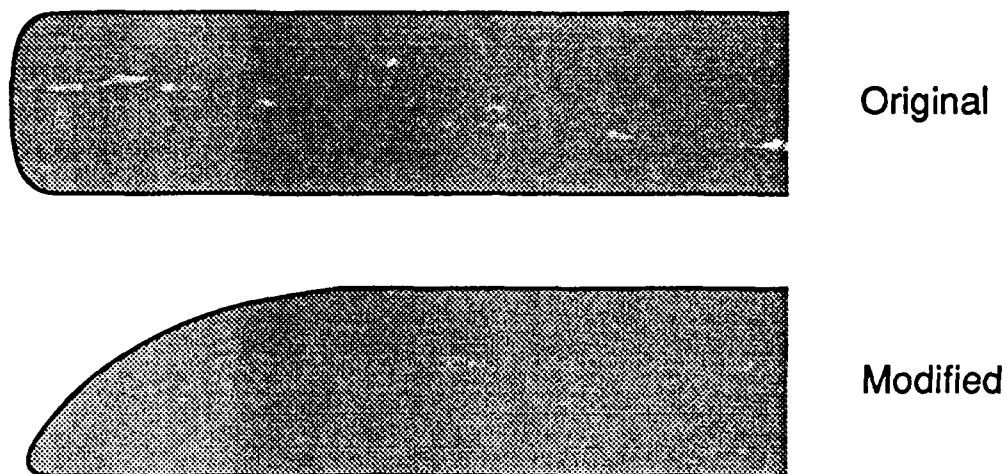
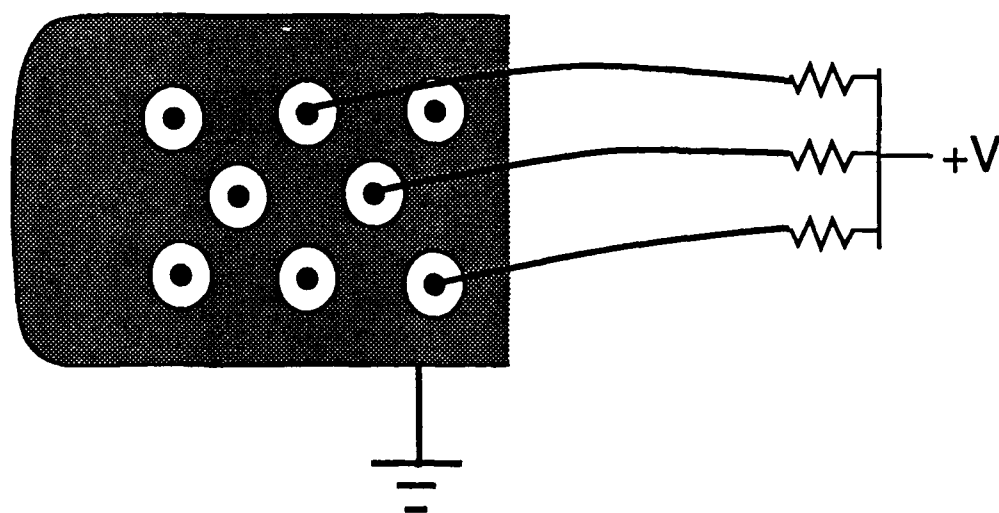


Figure 1.1: Assembly drawing of repetitively pulse CO₂ laser head



(A) Original and modified electrode profiles



(B) Schematic of preionization pins embedded in cathode.

Figure 1.2

completed and tested concurrently with the laser. The power system and the data system are described below.

1.2 Pulsed CO₂ Laser Driver

The design of the COLD-I (CO₂ Laser Driver) pulsed power supply has been presented in detail in a previous report. The COLD-I pulser is a compact, lightweight all-solid-state device employing SCR commutators combined with nonlinear magnetic pulse compression. During this reporting period, the pulser has been fabricated, tested, and incorporated into the laser discharge circuit. A photograph of the COLD-I pulser with a small laser head is shown in Fig. 1.3. The pulser operated properly, as expected. The I/V characteristics of the main discharge pulse are discussed below. A separate preionizing pulse is applied to the 22 wire pins immediately prior to the main pulse.

1.3 Diagnostics and Data System

Three diagnostic systems were installed to measure the discharge current, the discharge voltage, and the laser optical output power as functions of time. The current pulse is monitored by a Pierson wide band current transformer. The anode-cathode voltage is detected by a fiber optic voltage probe which is immune to troublesome inductive voltage swings on the nominally grounded anode. This probe, shown in Fig. 1.4, consists of two LED fiber optic transmitter/receiver loops. The resistor chain limits the current through the LED's to approximately 40 mA at the maximum voltage on the laser head. One LED will send out its light signal when the voltage across the laser head is positive and the other will send out its signal when the voltage difference is negative. There is a very small dead zone near zero voltage difference since the diodes require a volt or so of forward bias before any conduction occurs, but this is a tiny fraction of the kilovolt swings being measured. The diagnostic has an unambiguous ground reference and noise is reduced since there is no direct electrical connection between the LED voltage probes and the data acquisition system. This high voltage probe was shown to be linear up to at least 15 kV during calibration studies with a pulse generator. Reliable current and voltage measurements are obtained since both the voltage and current diagnostics are decoupled

150 JOULE 10 Hz CO₂ PULSER

CO₂ PULSER

PREIONIZER
ENERGY
STORAGE

LASER HEAD

PREIONIZER SPARK PLUGS

SCIENCE RESEARCH LABORATORY

Figure 1.3

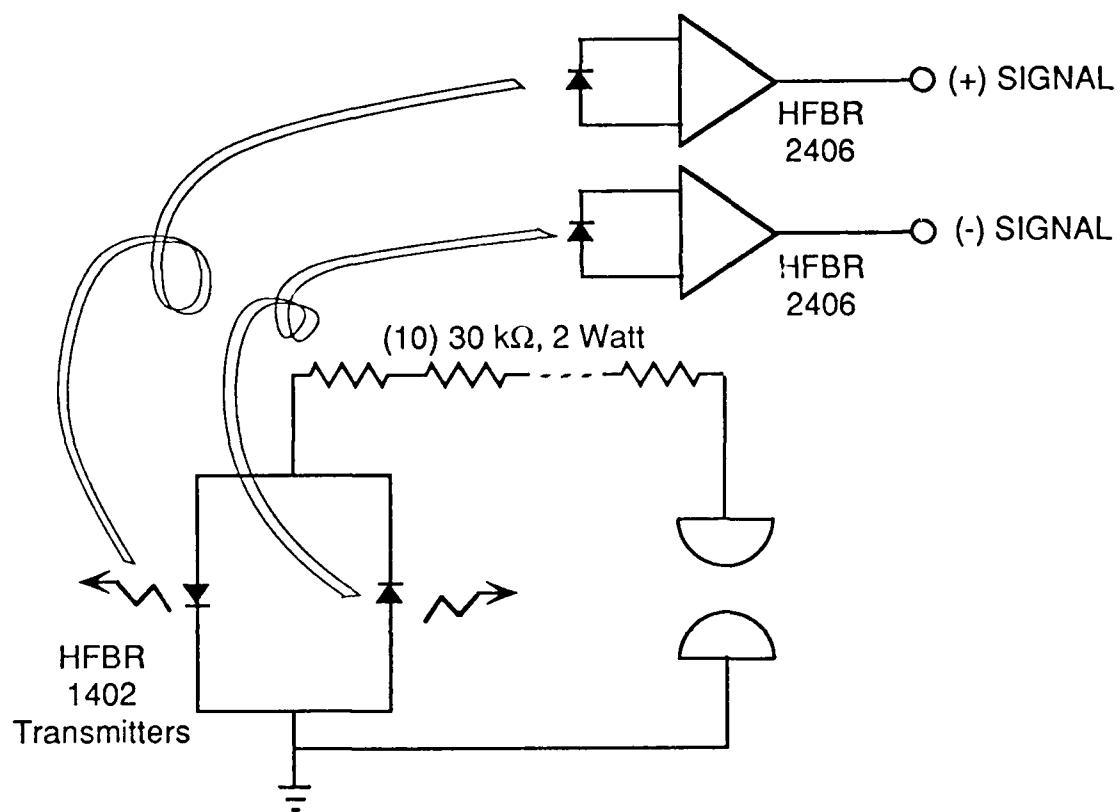


Figure 1.4

from the floating ground on the laser pulsed power supply.

Finally, the optical laser output pulseshape and energy are measured by a photon-drag detector with 1 nsec response time at the CO_2 wavelength and a pyroelectric energy meter, respectively. All diagnostic outputs are recorded by a data acquisition system assembled from modular CAMAC digitizers. Three 100 megasample sec^{-1} digitizers have been installed to read voltage, current and the laser pulseshape. Three 32 megasample sec^{-1} digitizers are available for monitoring the output of the pyroelectric energy meter and other test point voltages in the pulsed power system. A data acquisition program was written to program the digitizers, acquire the voltage traces and store the data in standardized file structures. The program provides for automatically generated, unique file names and appends descriptions of each test run to the individual data files. Provision has been made for recording 2-D images of beam profiles or of arc structure with a CCD camera if necessary.

1.4 Discharge Characteristics

After initial testing of the COLD-I pulsed power unit with CuSO_4 resistive loads ranging from 4 to 50 Ohms, the pulser was used to drive gas discharges in the laser head. With a 3:2:1 ($\text{He:N}_2:\text{CO}_2$) gas mixture, the response of the gaseous discharge to the pulser has been investigated intensively. Total gas pressures from 5 to 40 Torr have been studied. The input voltage to the pulser was varied from 500 to 1100 V; the discharge characteristics were found to be optimized at the higher input voltages.

Voltage and current traces from a 20 Torr discharge at 1000 V input are shown in Fig. 1.5. The peak output power to the discharge is 12 MW with an impedance of 4 Ohms. Voltage ringing during the first μsec is followed by a self-sustained discharge lasting an additional 2-3 μsec .

A 35 Torr discharge is shown in Fig. 1.6, also taken with 1000 V input to the COLD-I pulser. A numerical simulation of this discharge was performed to model the electron density and total current as a function of time. The simulation is based on two rate equations:

CO₂ Laser Discharge Characteristics

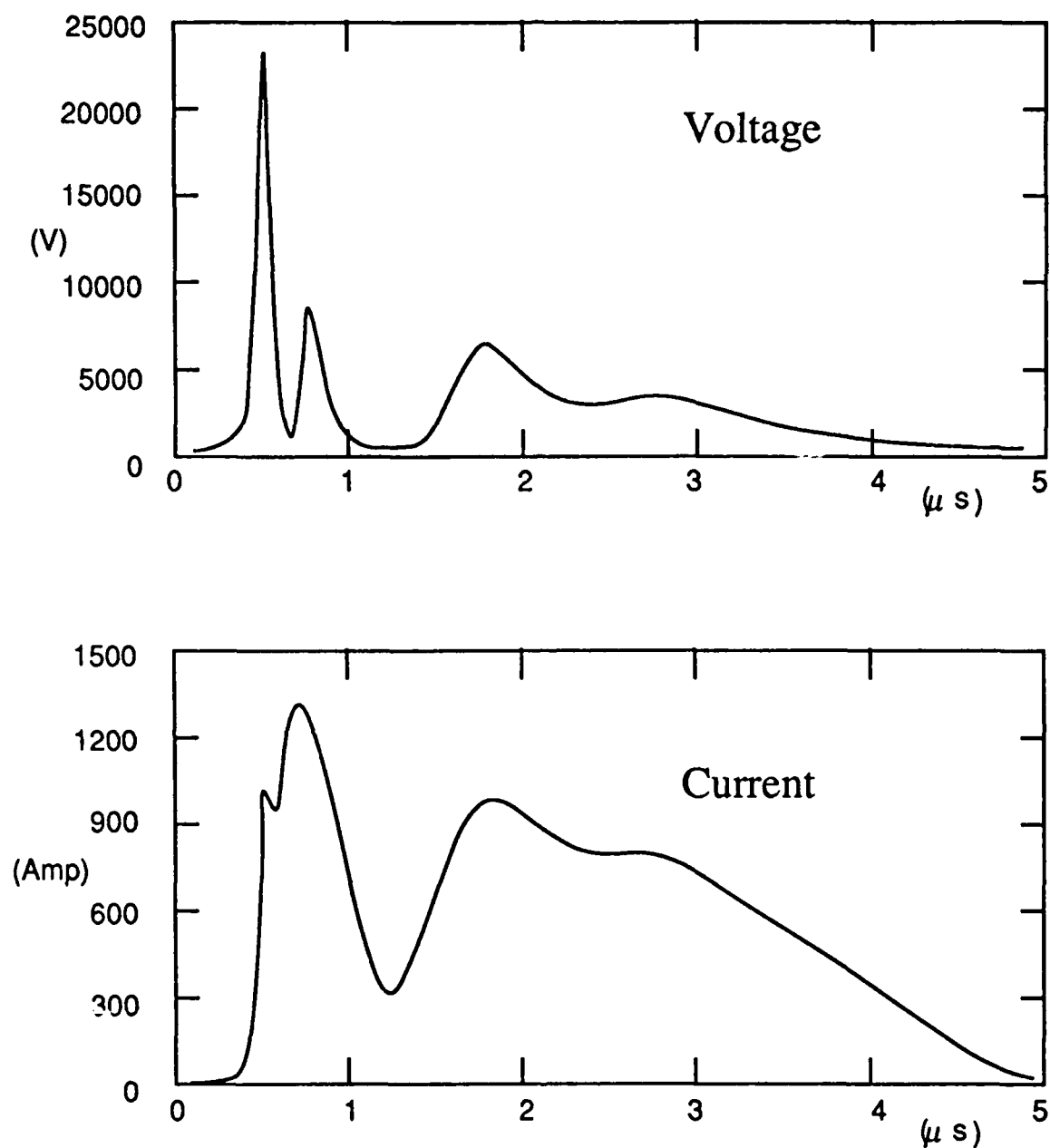


Figure 1.5 Voltage and current traces from 20 Torr discharge,

CO₂ Laser Discharge Characteristics

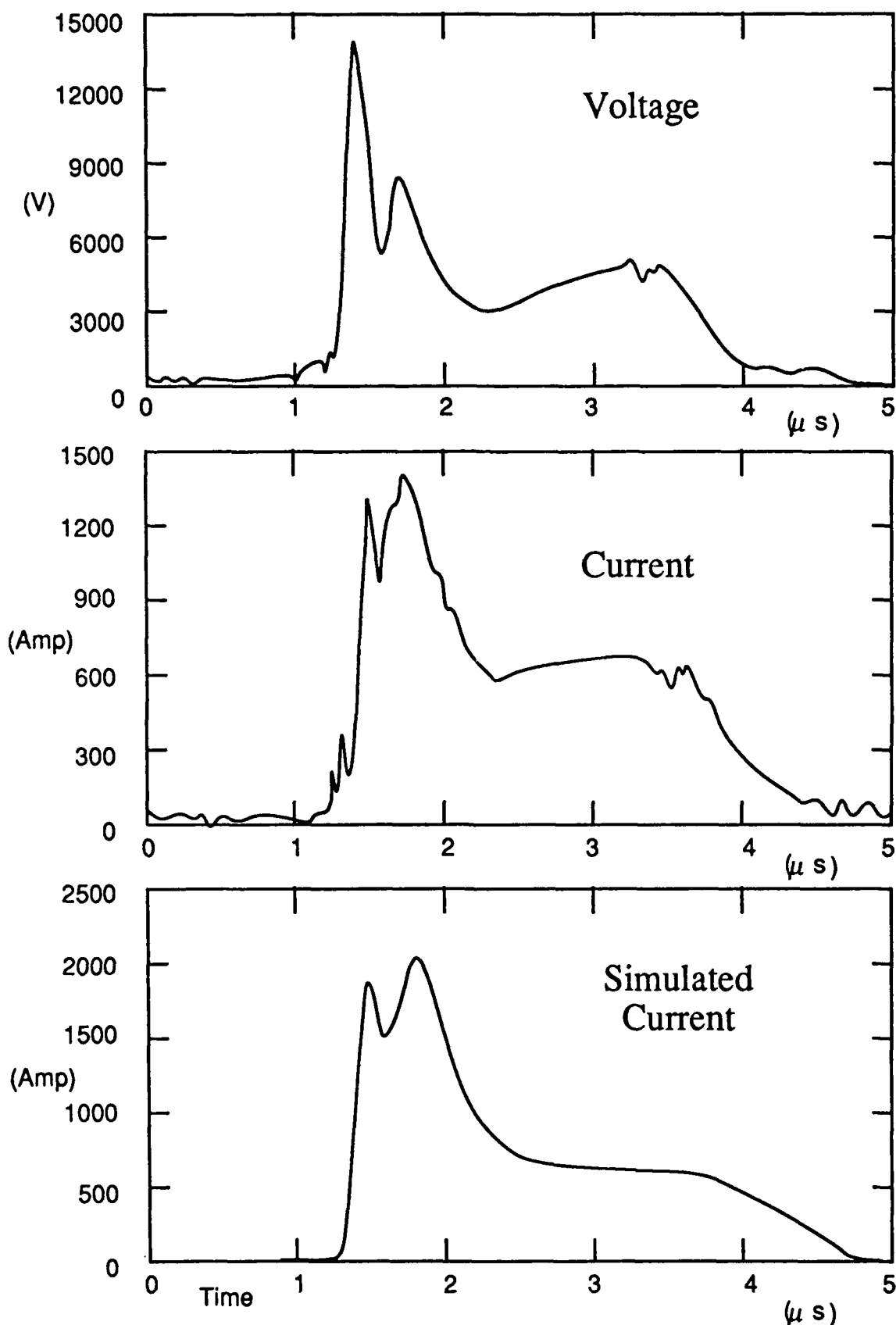


Figure 1.6 Voltage and current traces from 35 Torr discharge, including current predicted by numerical simulation.

$$\frac{dn_e}{dt} = \nu n_m n_e + \nu_a n_a n_e - \alpha n_e^2 - \beta n_e \quad (1.1)$$

and

$$\frac{dn_m}{dt} = \gamma n_e n_c - \frac{n_m}{\tau} \quad (1.2)$$

where n_e is the electron density, n_a the density of N_2 in the ground state, n_c the density of CO_2 in the ground state, n_m the density of CO_2 molecules in an electronic metastable state, ν the ionization rate of the metastable CO_2 , ν_a the ionization rate from the ground state of N_2 , α the ion-electron recombination rate, β the electron attachment rate, γ the collisional excitation rate for the metastable CO_2 , and τ is the lifetime of the metastables. From the electron density and voltage across the electrode one obtains the current through the electrode. The results of this simulation are also shown in Fig. 1.6. The close agreement between the simulation and experimental results suggest that Eqs. 1.1 and 1.2 describe the discharge process very well.

The discharge was stable and no arcs were observed along the insulators. An open shutter photograph of the 20 Torr discharge is shown in Fig. 1.7. From the photograph it is clear that the discharge current density is larger in the vicinity of the preionizers. The redesigned electrodes, which increase the number of preionization pins from 22 to 120, will improve the uniformity of the discharge.

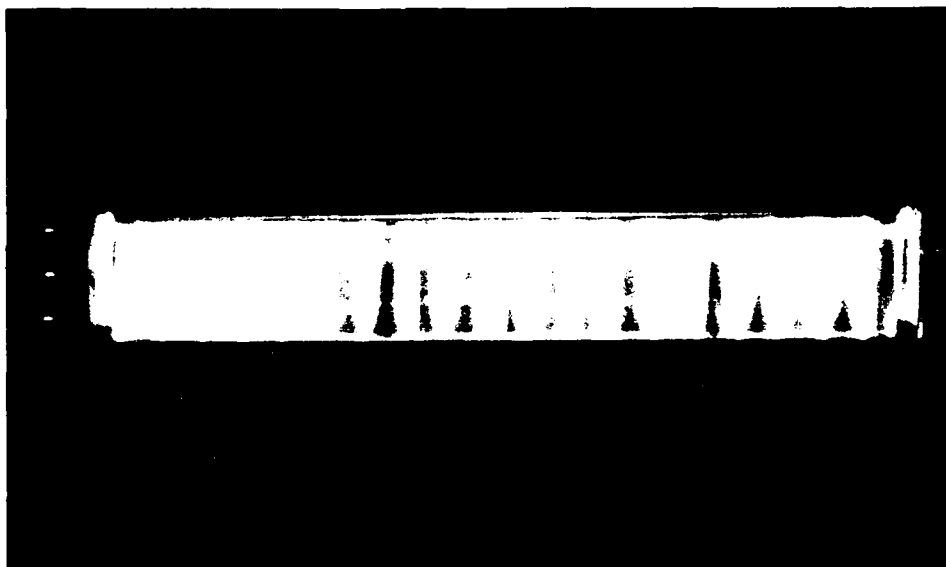
1.5 Laser Performance Results

The CO_2 laser cavity consists of a molybdenum back mirror (uncoated) having a 10 meter radius of curvature and a ZnS 50% transmission output coupler (AR coated). Typical laser outputs are shown and compared to numerical simulations for the 20 Torr and 35 Torr discharges discussed above in Figs. 1.8 and 1.9, respectively.

At 20 Torr (Fig. 1.8), the observed laser output decays exponentially with a time constant of 28 μsec , which corresponds to the collisional energy transfer time between N_2 and CO_2 . This is in good agreement with the numerical simulation for that pressure, which exhibits a decay time of 25 μsec .

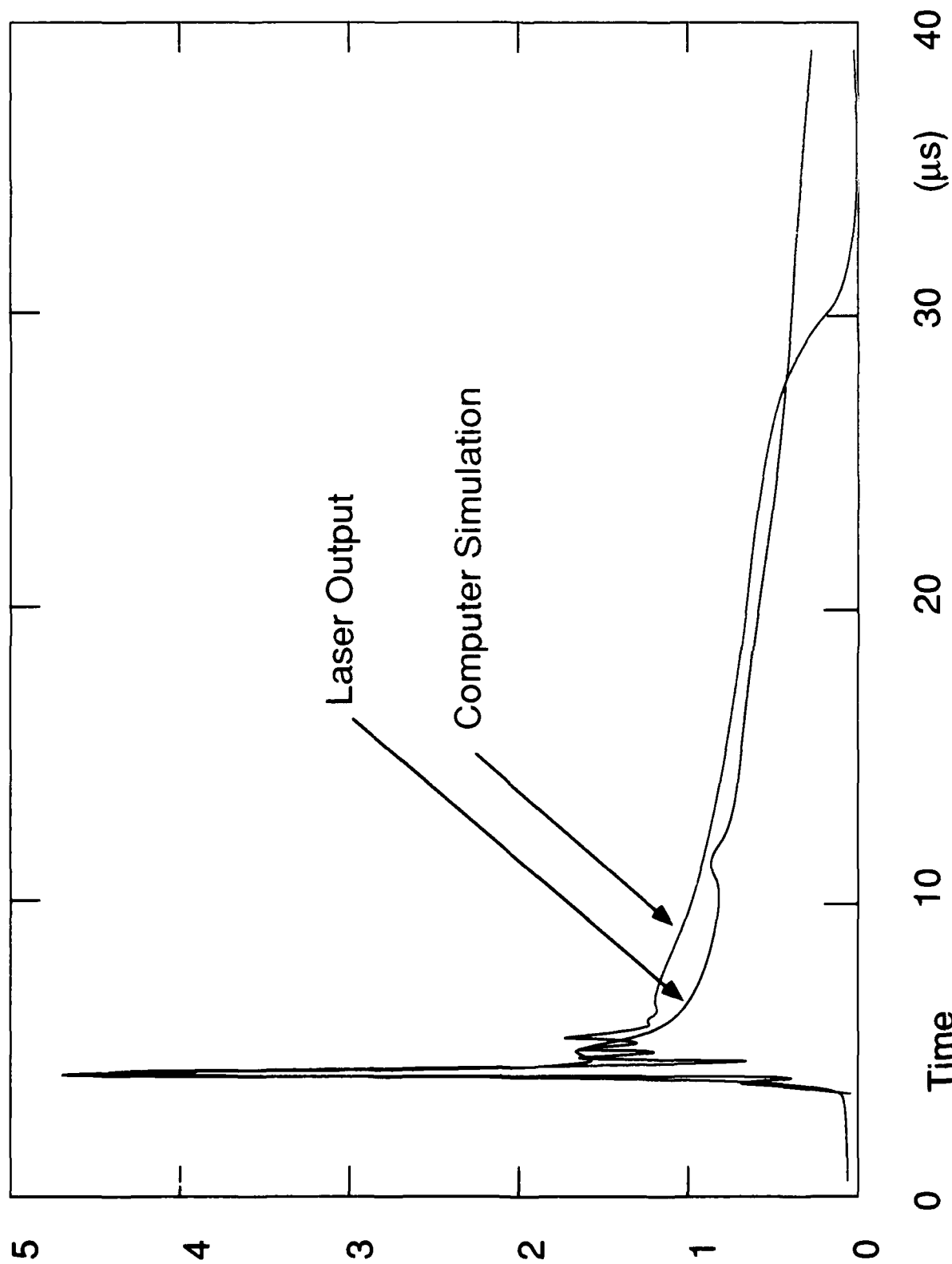
At 35 Torr (Fig. 1.9), the laser output builds up on a 2 μsec time scale after the initial 0.5

CONDUCTION COOLED CO₂ LASER DISCHARGE



Active Volume	$2.0 \times 13.5 \times 100 \text{ cm}^3$
Voltage	5 kV
Electrode Spacing	13.5 cm
Current	800 Amps
Discharge Pulse Length	$3 \mu\text{s}$
Laser Pulse Length	$40 \mu\text{s}$
Overall Efficiency	14%
Total Gas Pressure	30 Torr

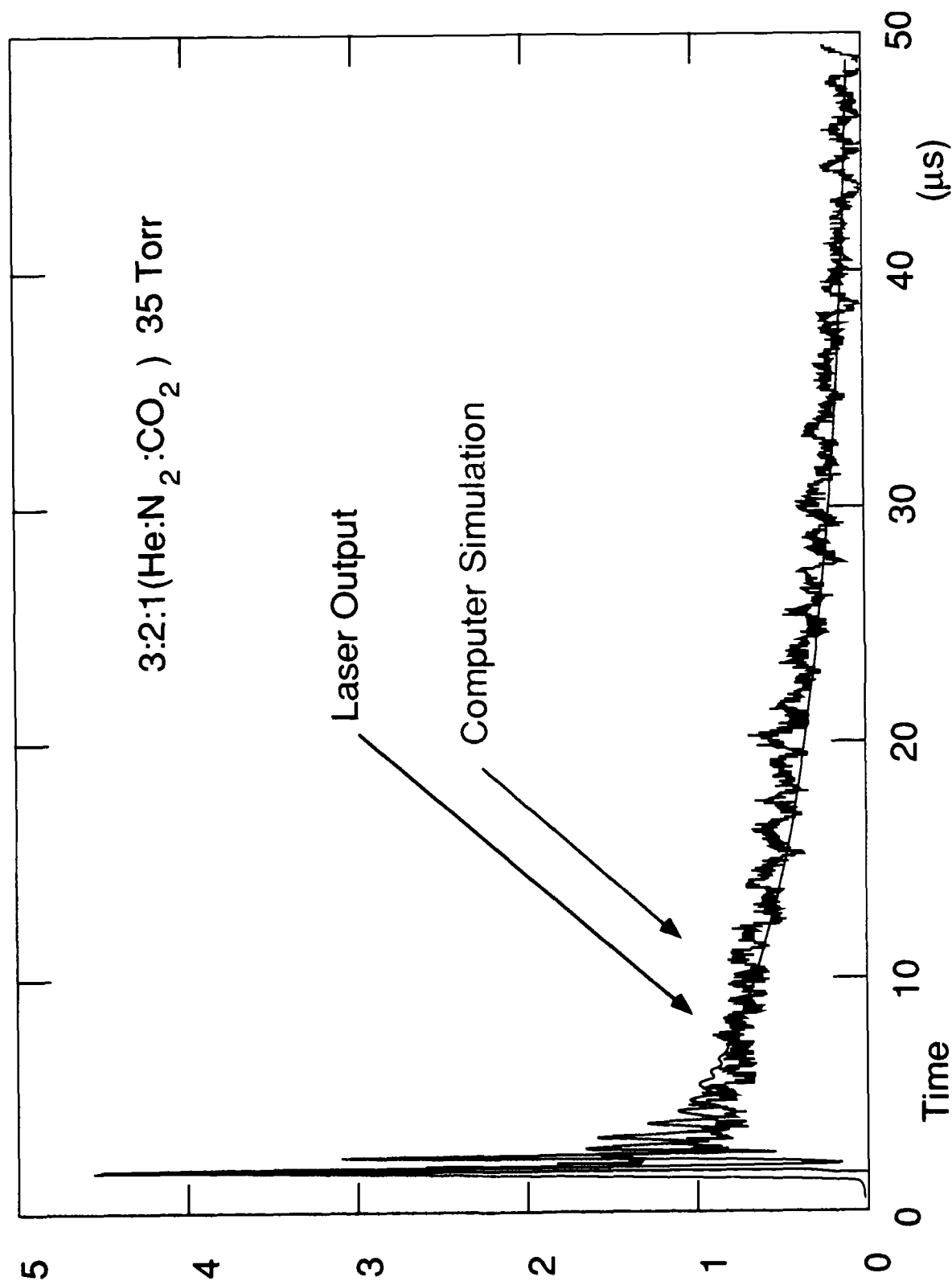
Figure 1.7



04/1/90

Figure 1.8

SCIENCE RESEARCH LABORATORY



64J190

Figure 1.9

SCIENCE RESEARCH LABORATORY

μsec spike, and has an exponential decay time of $21 \mu\text{sec}$ due to the faster collision rate. The tail of the pulse is over $40 \mu\text{sec}$ long. This agrees very well with the simulated pulse shape, which has a decay time of $16.4 \mu\text{sec}$. The simulation exhibits more ringing of the pulse after the initial spike than is detected experimentally. The maximum total laser output energy is 600 mJ, corresponding to a conversion efficiency of 14%.

SECTION 2

2.0 LASER DISCHARGE STABILIZATION

2.1 Introduction

In previous reports, SRL has presented a stability model for one-dimensional DC volumetric discharges. Stability was found to depend critically on the electron attachment rate constant (β) for several operating regimes. In this section, those results are summarized and extended in terms of the critical electric field required for stable operation in each regime. Kinetic rate coefficients previously calculated and reported for a one atmosphere total pressure, 3:2:1 (He:N₂:CO₂) mixture are used in numerical calculations presented below.

In addition to the DC stability model, SRL has developed a two-dimensional model for RF discharges which demonstrates the possibility of inductive stabilization of the discharge against streamer formation. This model, reported previously, has now been incorporated into a numerical code and used to predict discharge behavior under conditions of RF electric fields. These new results are presented in Section 2.5 below.

The stability of high pressure discharges has been a subject of major concern in the high power laser community over the last fifteen years. Most of the discharge stability research, especially for CO₂ laser discharges, concentrated on thermal instabilities and their effect on the constriction and arcing of the discharge. Vibrational stabilization methods have been proposed to suppress these instabilities.

The thermal instabilities, by their nature, can only develop on acoustic (millisecond) time scales. However, in many cases arcing occurs on a much faster (micro-second and submicrosecond) scale. The phenomenon is characteristic of systems where the electron loss by attachment is present and the two-step electron impact ionization is dominant. Such a model successfully explained the experimentally observed temporally rapid instability scales in the KrF laser discharges.

In addition to the KrF laser discharge case, subacoustic arcing time scales have been also observed in the high power CO₂ laser experiments. An example of such arcing is in connection

with the gas recirculation in the laser, resulting in the buildup of the attaching oxygen component in the laser gas mixture. These observations could also be explained within the two-step ionization model. Although the details of the kinetics in a high pressure molecular discharge are complex, the concept of two-step ionization as the dominant ionization source in the discharge is plausible. The basic reason stems from the fact that the electron temperature in these discharges is relatively low (typically 1-2 electron volts) and very few electrons in the tail of the distribution function can directly ionize the ground state, while the ionization of a variety of available excited and metastable states requires much lower energies and is accessible by the bulk of the electron energy distribution. It is precisely this reason which makes the further development of the multi-step ionization discharge theory necessary.

2.2 The Steady State Solution

Consider a system, shown schematically in Fig. 2.1 with a DC voltage source V_0 . The voltage is distributed between the external resistor R and the plasma, so that

$$V_0 = RI + LE \quad (2.1)$$

where I is the discharge current, L is the plasma length and E is the electric field in the plasma, which is assumed to be uniform at all times. In writing Eq.(2.1) it is assumed that the cathode fall voltage is negligible compared to LE (a situation typical of *high pressure* discharges).

Three regimes of operation will be investigated:

A. Stiff Voltage Case - Here $R \simeq 0$ and thus the field in the discharge

$$E = \frac{V_0}{L} = \text{Const} \quad (2.2)$$

is not affected by a possible time variation of discharge characteristics, such as the electron density, temperature etc.

B. Stiff Current Case - In this case $R \rightarrow \infty$ and $V_0 \rightarrow \infty$, so that the current

$$I \simeq \frac{V_0}{R} = \text{const} \quad (2.3)$$

is time independent and fully described by the external circuit.

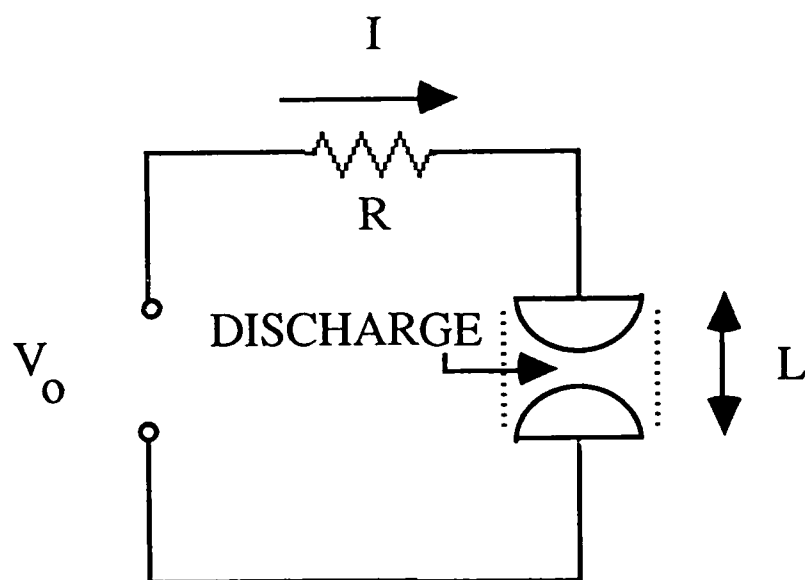


Figure 2.1: General circuit model.

C. Finite External Impedance Case - In this intermediate case ($0 < R < \infty$) both the current

$$I(t) = \frac{V_0 - LE(t)}{R} \quad (2.4)$$

and the electric field $E(t)$ depend on the details of the time evolution of the discharge.

At this point it is necessary to discuss the kinetics of the self-sustained discharge. The densities of various species in the discharge will be assumed to be spatially uniform, and the discharge is described by the following system of rate equations

$$\frac{dn_e}{dt} = \nu n_m n_e - \alpha n_e^2 - \beta n_e \quad (2.5)$$

$$\frac{dn_m}{dt} = \gamma n_e n_a - \frac{n_m}{\tau} \quad (2.6)$$

Here n_e is the electron density, governed by the ionization of an excited or metastable state having a density n_m and by recombination and attachment losses (ν , α and β are the corresponding rate constants). The density of the excited or metastable state is defined by the balance between the processes of the excitation by electron impact of atoms from the ground state (of density n_a) and the collisional quenching by the neutral gas (with characteristic time constant τ). The time scales τ , (αn_e) and β^{-1} are assumed to be much shorter than the acoustic times and thus the neutral gas temperature and density are constants.

Equations (2.5) and (2.6) yield the steady state in which all the discharge characteristics are constant and

$$n_m = n_{m0} = \gamma_0 \tau n_{e0} n_a \quad (2.7)$$

$$n_e = n_{e0} = \frac{\beta_0}{(\nu_0 \gamma_0 \tau n_a - \alpha_0)} \quad (2.8)$$

The question of whether this steady state can be reached for a given set of parameters of the external circuit (V_0 , R and L) will be considered next. The answer to this question depends on the regime of operation:

A. Stiff Voltage Case - Here $E = E_0$ is given, which defines all the rates in Eq. (A.8) so that n_{e0} is known. This, in turn, defines the current density $j = en_{e0}v_{d0}$ in the plasma

(v_{do} being the drift velocity of the electrons). Thus the steady state exists, provided of course (see Eq. (2.8)) the quantity

$$Q(E_o) \equiv \nu_o \gamma_o \tau n_a - \alpha_o \quad (2.9)$$

is *positive*. This condition restricts the accessibility of the steady state and needs a further discussion. Consider the dependence of Q on E_o . Typically, the excitation and ionization rates (γ_o, ν_o) are increasing functions of the electric field, while the attachment rate α_o normally decreases with E_o . Furthermore, $\lim_{E_o \rightarrow 0} Q \simeq -\alpha_{(E_o=0)} < 0$ and with the increase of E_o , $Q \rightarrow \nu_o \gamma_o \tau n_a > 0$. Therefore there exists a *single* value of the electric field $E_o = E^*$ at which $Q(E^*) = 0$. The steady state operation of the discharge under the stiff voltage conditions (E_o is given) is thus only possible when

$$E_o \simeq \frac{V_o}{L} > E^* \quad (2.10)$$

B. Stiff Current Case - Here the current I_o is defined by the external circuit. On the other hand from Eq. (2.8)

$$I_o = e v_{do} n_{eo} S = \frac{e v_{do} \beta_o S}{Q(E_o)} \equiv F(E_o) \quad (2.11)$$

where S is the cross section area of the discharge. Equation (2.11) now defines the steady state electric field value E_o . A graphical illustration of the solution of this equation is given in Fig. 2.2, where the qualitative dependence of function F on E is shown based on our earlier discussion of function $Q(E)$. A possible minimum of F at $E = E_m$ is also shown. Such a minimum may exist at high values of E_o at which the ionization and excitation rates grow slower than the drift velocity v_d as the electric field increases. It can be seen in Fig. 2.2 that the steady state exists for any current I_o , provided it is larger than I_m . It is noteworthy that the operation near E_o^* requires rather high currents.

C. Finite Impedance Case - In this intermediate case Eq.(2.11) is replaced by (see Eq. (2.4) for the current)

$$\frac{V_o - L E_o}{R} = F(E_o) \quad (2.12)$$

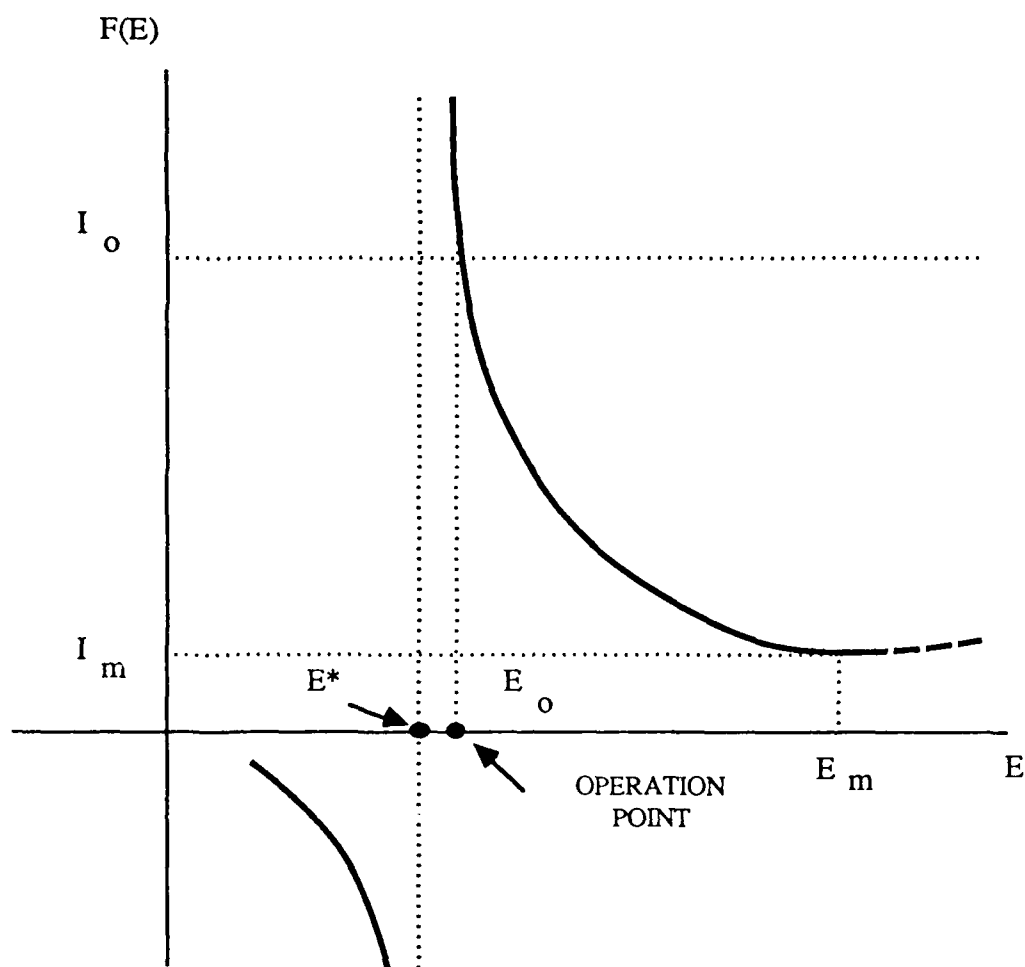


Figure 2.2: Graphical solution for the electric field in the discharge under stiff current condition (I_0 is given).

The graphical solution of this equation for E_o is shown in Fig. 2.3. One observes that for given values of V_o there exists a critical impedance R_{cr} such that when $R < R_{cr}$ two steady state solutions (E_{o1} and E_{o2}) exist for the electric field, while for $R > R_{cr}$ no steady state exists at all. For $R = R_{cr}$ there is a single steady state. The value of R_{cr} can be found from

$$L = -R_{cr}F'(E_{cr}) \quad (2.13)$$

where $F' = dF/dE_o$ and E_{cr} is given implicitly by

$$E_{cr} - \frac{V_o}{L} = \frac{F(E_{cr})}{F'(E_{cr})} \quad (2.14)$$

This completes the analysis of the possibility of a steady state solution at various external circuit conditions.

2.3 Numerical Example

At this stage the stability of the discharge at various operating conditions will be analysed. The analysis will be started by presenting the dependence of function $F(E)/S$ on the electric field (see Eq. (2.11)). This dependence is shown in Fig. 2.4 for the case of interest. One observes that $E^* \simeq 8.05$ kV/cm, so that the steady state discharge operation is possible for $8.05 \text{ kV/cm} < E < 15 \text{ kV/cm}$ (see the discussion in Section 2.2 and Figs. 2.2 and 2.3). The graphical solution for the electric field E_o in the steady state discharge is also shown under the following conditions: $V_o = 9 \text{ kV}$, $RS = 400 \Omega\text{cm}^2$, $L = 1 \text{ cm}$, $\tau = 1 \mu\text{sec}$ and $\beta_o = 10^5 \text{ sec}^{-1}$. The steady state electric field is 8.45 kV/cm which, by using Eq. (2.8), and rate coefficients appropriate for the 1 atm, 3:2:1 (He:N₂:CO₂) gas mixture (determined previously as function of E), yields the steady state plasma density $n_{eo} = 1.07 \cdot 10^{12} \text{cm}^{-3}$. Prior to studying the stability of the discharge at these conditions, the stiff voltage situation is considered. Previously reported analysis showed that the discharge is *unstable* in the stiff voltage case for $\beta_o \neq 0$. This unstable behavior is demonstrated in Figs. 2.5 and 2.6, where the numerical solutions of Eqs. (2.5) and (2.6) are shown for $E_o = 8.45 \text{ kV/cm} = \text{Const}(t)$ (stiff voltage condition) and two different initial values for the electron density. The electric field E_o defines various rates in Eqs. (2.5) and

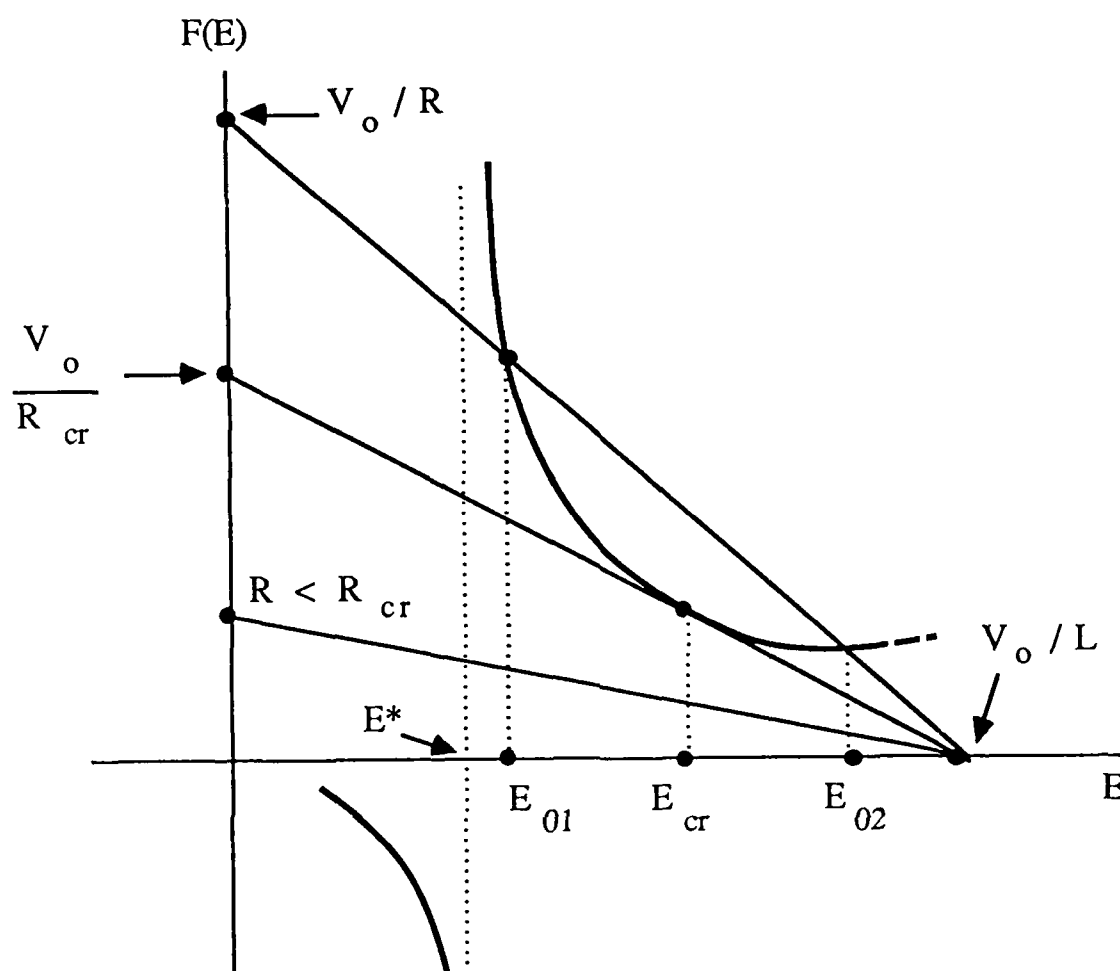


Figure 2.3: Graphical solution for the electric field E_0 in the discharge under finite impedance conditions. The straight lines describe the function $(V_0 - LE_0)/R$ for different values of the external impedance R .

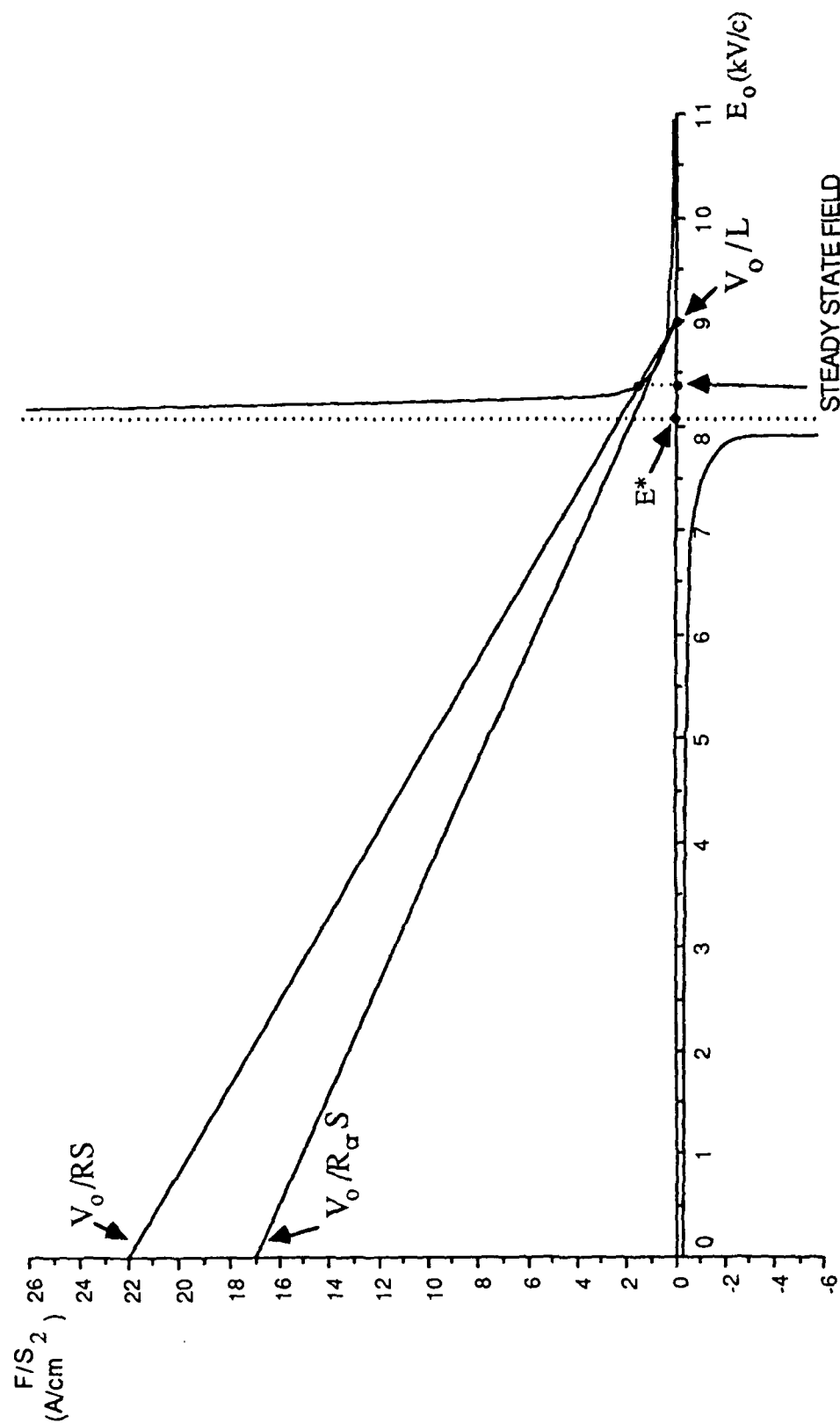


Figure 2.4: The dependence of F/S on the electric field in a 1 atm, CO_2 laser discharge mixture. The operating field ($E_0 = 8.45$ kV/cm found graphically for the case: $V_0 = 9$ kV/cm, $RS = 400 \Omega \text{ cm}^2$, $L = 1$ cm, $\tau = 1 \mu\text{sec}$, and $\beta_0 = 10^5 \text{ sec}^{-1}$). The straight line tangent to the curve F/S allows to determine

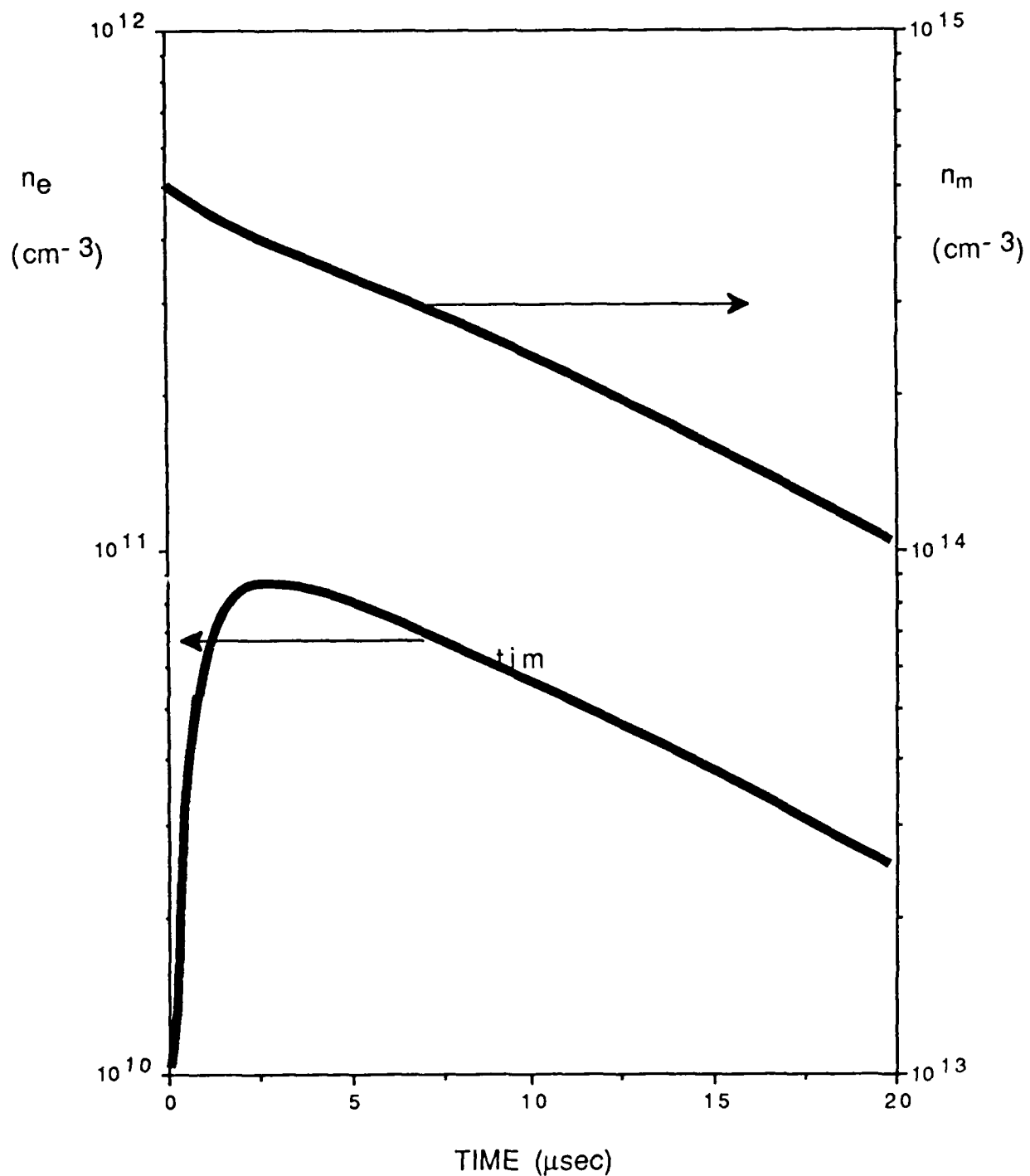


Figure 2.5: The time evolution of the electron and metastable densities in a stiff voltage discharge. The initial electron density ($n_e(0) = 5 \times 10^{11} \text{ cm}^{-3}$) is lower than the steady state density ($n_{\infty} = 1.07 \times 10^{12} \text{ cm}^{-3}$) at the given voltage ($V_0 = 8.45 \text{ kV}$).

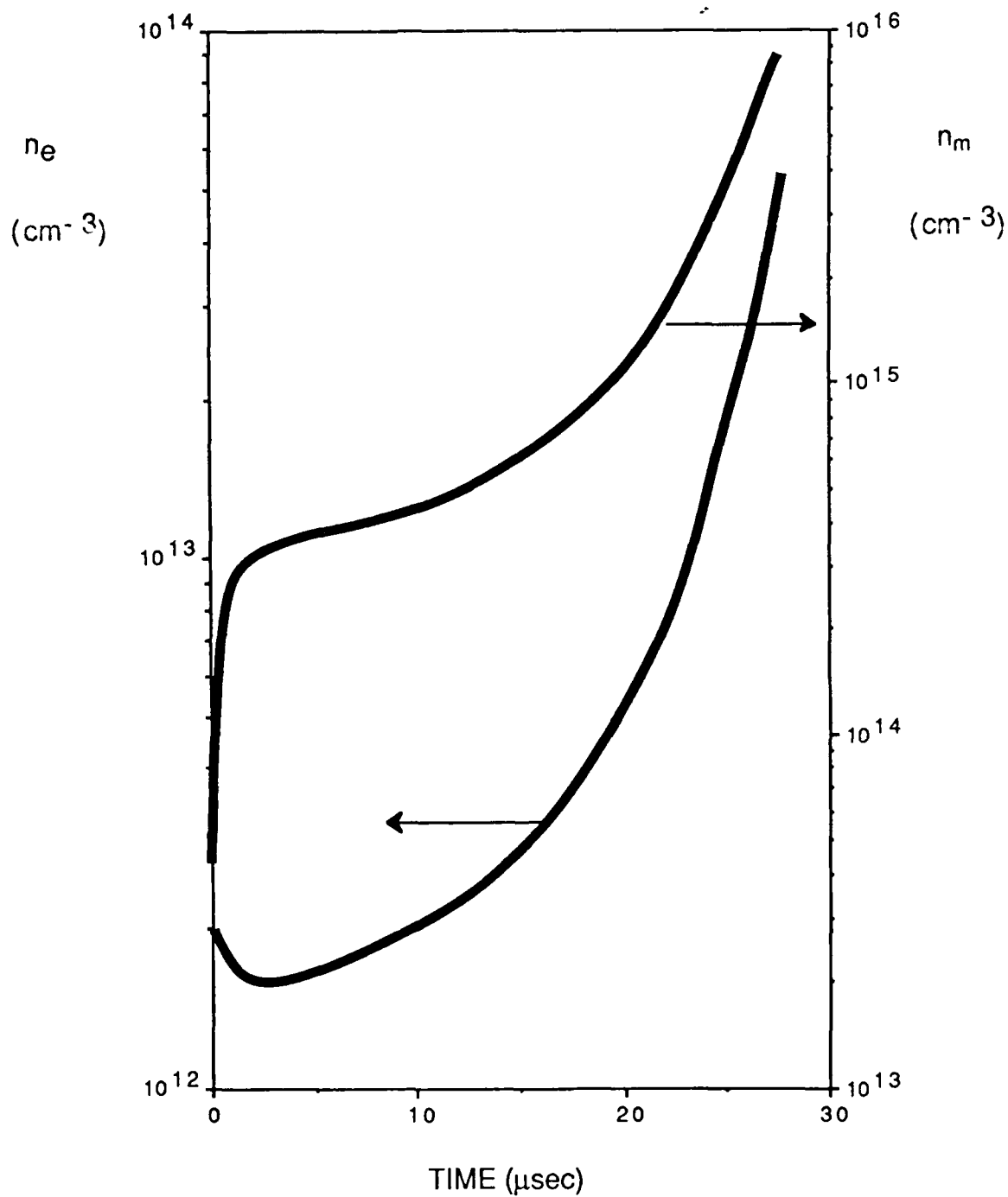


Figure 2.6: The time evolution of the electron and metastable densities in a stiff voltage discharge with attachment. Initial electron density ($2 \times 10^{12} \text{ cm}^{-3}$) is higher than the steady state density ($n_{\infty} = 1.07 \times 10^{12} \text{ cm}^{-3}$) at the given voltage ($V_0 = 8.45 \text{ kV}$).

(2.6) which remain constants in the calculations, consistent with the stiff voltage conditions. Figure 2.5 shows the case when $n_e(0) = n_m(0) = 5 \cdot 10^{11} \text{cm}^{-3}$. This initial density is lower than the above mentioned steady state density ($n_{eo} = 1.07 \cdot 10^{12} \text{cm}^{-3}$). Figure 2.5 shows that the electron density decays in time, in this case, and the discharge is quenched. Figure 2.6, in contrast, shows the case of $n_e(o) = n_m(o) = 2 \cdot 10^{12} \text{cm}^{-3}$ which is larger than the steady state electron density n_{eo} . n_e then grows indefinitely in time, verifying the instability. One finds that Figs. 2.5 and 2.6 represent the general time evolution of the discharge in the stiff voltage case, depending on whether $n_e(o)$ is larger or smaller than n_{eo} .

At this point it is appropriate to proceed to the numerical simulation of the finite external impedance discharge case, again setting $V_o = 9 \text{ kV/cm}$, $L = 1 \text{ cm}$, $\tau = 1 \mu\text{sec}$ and $\beta = 10^5 \text{ sec}^{-1} = \text{Const}(t)$. Nevertheless, in contrast to the stiff voltage case, the rate Eqs. (2.5) and (2.6) have now been solved simultaneously with the circuit Eq. (2.14). The code also makes use of the dependencies of the CO_2 gas mixture rate constants determined previously. The predictions of the code are plotted in Figs. 2.7, 2.8 and 2.9. Figure 2.7 shows the temporal variation of n_e and E for the circuit impedance of $RS = 400 \Omega \text{cm}^2$. The initial electron density was assumed to be 10^{12}cm^{-3} . One observes that the electron density increases by about 10% to $1.07 \cdot 10^{12} \text{cm}^{-3}$ and the electric field decreases from its initial value of 9 kV/cm to 8.45 kV/cm . These are the steady state electron density and the electric field under the above conditions. Figure 2.8 shows the effect of lowering the external impedance to $RS = 1 \Omega \text{cm}^2$. Under these conditions, as can be seen in the figure, the discharge has stiff voltage characteristics during the first $\sim 10 \mu\text{sec}$ of the discharge. It is unstable as predicted by the analysis and the electron density suddenly increases by almost three orders of magnitude after $10 \mu\text{sec}$. The discharge becomes stable at this large value of $n_e \sim 8 \cdot 10^{14} \text{cm}^{-3}$. However, in practice, any initial spatial nonuniformities in n_e amplified in time by the instability could result in streamer formation during the fast transition period. We shall consider the details of such spatial instabilities in the next chapter of this report. Finally, Fig. 2.9 illustrates a typically situation in a discharge with an above-critical external impedance ($R > R_{cr}$, see the discussion in the previous section). In the case considered

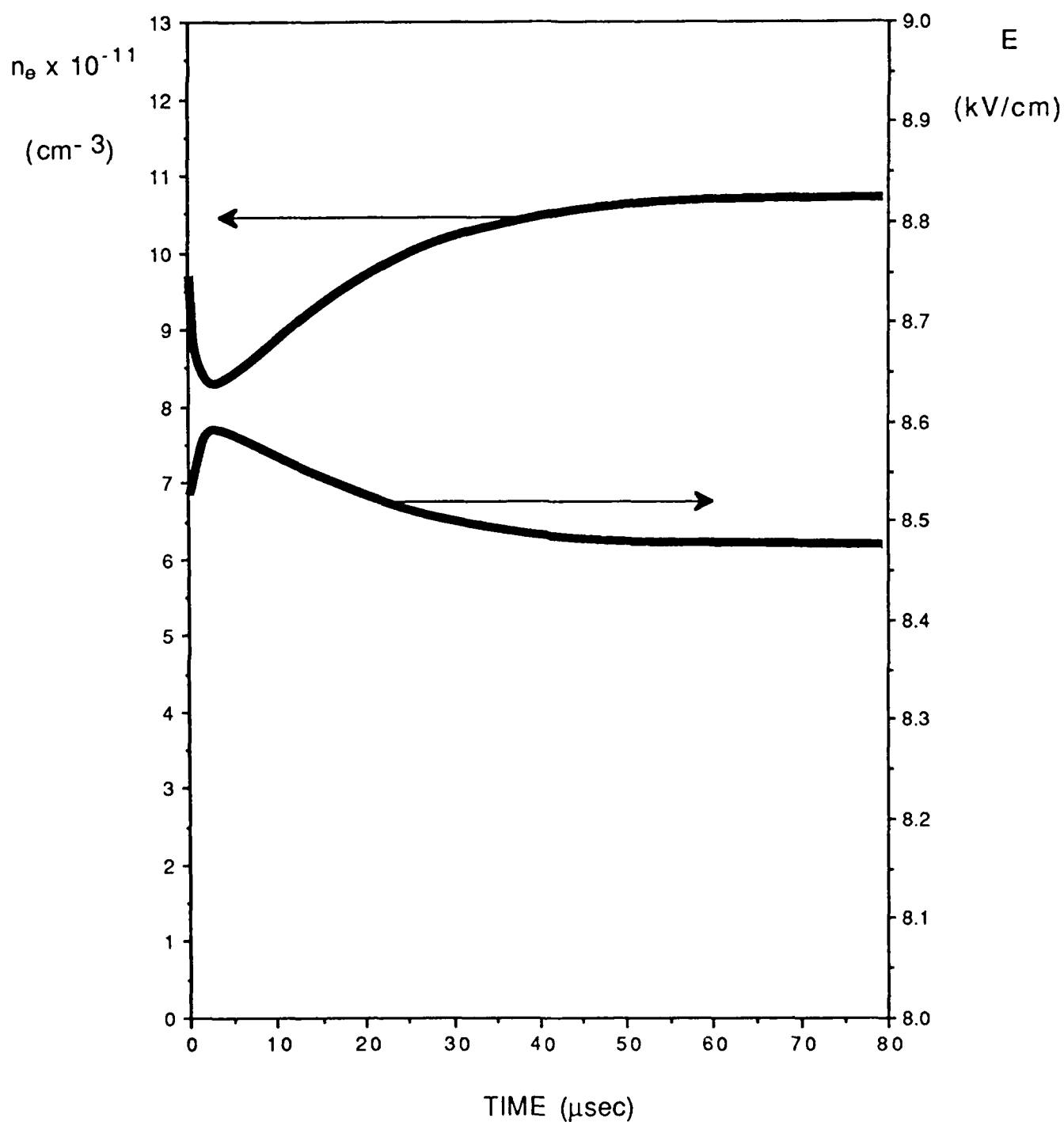


Figure 2.7: Curves of n_e and E for a volumetrically stable discharge. The parameters are: $n_e(0) = 10^{12} \text{ cm}^{-3}$, $V_0 = 9 \text{ kV/cm}$, $RS = 400 \Omega \text{ cm}^2$, $l = 1 \text{ cm}$, $\tau = 1 \mu\text{sec}$, $\beta = 10^5 \text{ sec}^{-1}$.

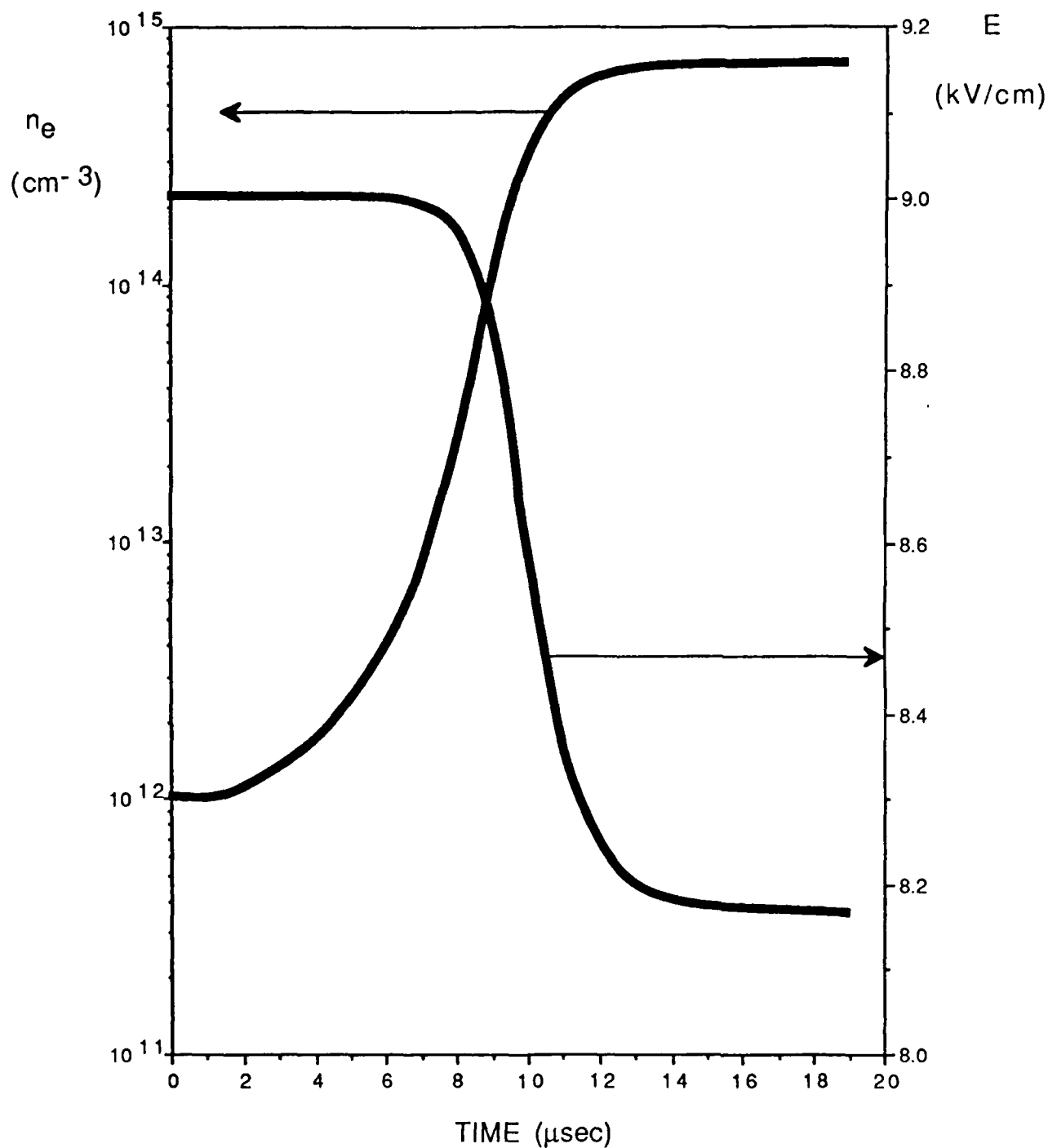


Figure 2.8: Curves of n_e and E for a low external impedance discharge ($RS = 1 \text{ W cm}^2$). The parameters are $n_e(0) = 10^{12} \text{ cm}^{-3}$, $V_0 = 9 \text{ kV/cm}$, $L = 1 \text{ cm}$, $t = 1 \text{ msec}$ and $b = 10^5 \text{ sec}^{-1}$. The discharge is unstable during the initial evolution phase ($t < 15 \text{ msec}$).

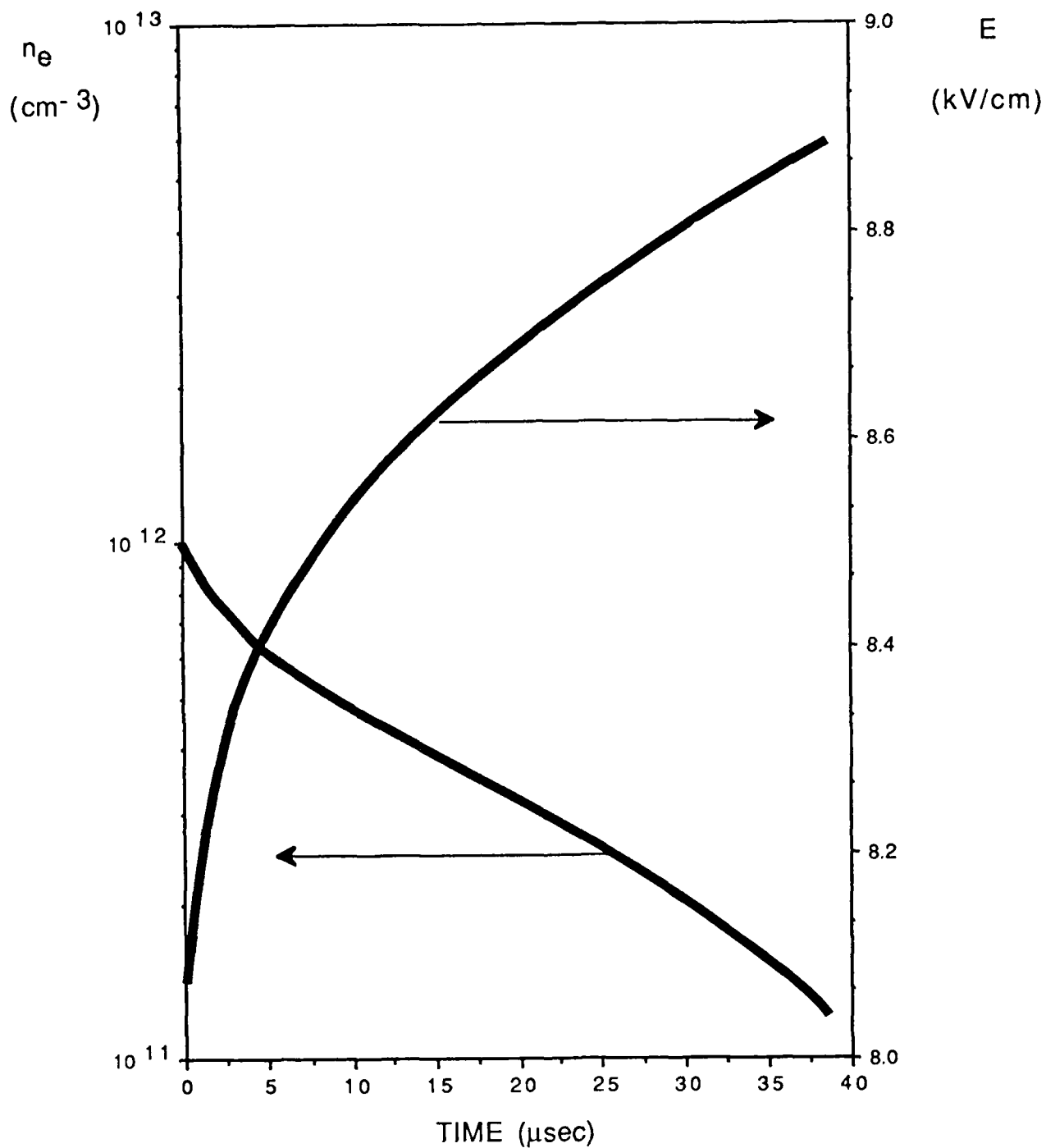


Figure 2.9: The curves of n_e and E for a discharge with an above- critical impedance ($RS = 800 \Omega \text{ cm}^2$). All other parameters are the same as in Figs. 3.10 and 3.11. No steady state exists for $RS > R_{\alpha}S = 520 \Omega \text{ cm}^2$ and the discharge is quenched.

(see Fig. 2.4) $R_{cr} \simeq 520 \Omega\text{cm}^2$, while the results presented in Fig. 2.9 correspond to the case $R = 800 \Omega\text{cm}^2$. No steady state exists in this case, as predicted by the theory, and one observes in Fig. 2.9 that the discharge is quenched.

2.4 Stability Conclusions

- (i) We have considered the volumetric stability dynamics of discharges dominated by **two step ionization**. In the presence of an attacher these discharges are shown to be potentially unstable on much shorter time scales than those characteristic of conventional thermal instabilities.
- (ii) The theoretical modeling of the discharge included the discharge kinetics coupled to the **external electric circuit** and its response to varying current conditions. A number of discharge configurations, such as stiff voltage, stiff current and finite external impedance were considered in searching for a steady state stable regime of operation.
- (iii) In the stiff voltage discharge [the electric field in the discharge $E = \text{const}(t)$] the steady state exists for $E > E^*$, where E^* is the value at which the characteristic function $Q(E)$ [see Eq. (2.9)] vanishes. Nevertheless, even if the steady state is reached, the discharge is volumetrically unstable under the stiff voltage condition. Practically, if at $t = 0$ the initial electron density $n_e(0) > n_{eo}$ (n_{eo} being the steady state density) the current density j increases indefinitely on a finite time scale, while for $n_e(0) < n_{eo}$ the discharge is quenched ($j(+) \rightarrow 0$). The linear instability temporal rate is typically proportional to the attachment rate β (if β is sufficiently small).
- (iv) The stiff current discharge [$j = \text{const}(t)$] has a steady state at **all** currents and the discharge is volumetrically stable, provided the characteristic function $F(E)$ [see Eq. (2.11)] is **decreasing** function of the electric field.
- (v) In the finite external impedance discharge case we found the existence of a critical impedance value R_{cr} such that there exist two steady state when $0 < R < R_{cr}$ and no steady state is possible when $R > R_{cr}$. Furthermore, only if R_{cr} is large enough, the above mentioned steady state solutions are stable in a part of the interval $[0, R_{cr}]$.
- (vi) The theoretical predictions were illustrated in the example of an atmospheric CO_2 laser

discharge model. The numerical solutions of the kinetic and external circuit equations, underlying the problem in this case were found in an agreement with the theory.

2.5 Numerical Simulations of The Two Dimensional Code

SRL has developed a code based on the two dimensional RF discharge theory presented in a previous report. The basic equation in rectilinear coordinates is

$$\frac{\partial^2 E}{\partial x^2} + \frac{i4\pi e^2 n_{eo}}{mc^2} \frac{\omega}{\nu_{coll}} E_o = 0 \quad (2.15)$$

subject to the boundary conditions

$$\frac{\partial E}{\partial x} \Big|_{x=0} = 0 \quad \text{and} \quad \frac{\partial E}{\partial x} \Big|_{x=w} = -\frac{2\omega I_o}{c^2}$$

where I_o is the total current per unit length. Equation (2.15) is valid for a slab geometry i.e. where the z dimension is much longer than x - dimension. Such a geometry conforms more to the CO_2 lasers than the radial geometry. It is assumed that the frequency of oscillation $f \gg \alpha n_e$, hence the electron density will remain essentially constant during a period of oscillation. This allows one to use time averaged rates for α , ν and $\langle \sigma v \rangle$. These time averaged rates are defined by the following integral

$$\bar{\xi} = \frac{\omega}{\pi} \int_0^{\pi/\omega} \xi(|E| \sin \omega t) dt = \frac{1}{\pi} \int_0^{\pi} \xi(E_o \sin s) ds = \bar{\xi}(|E|) \quad (2.16)$$

where $\xi = \nu$, α and $\langle \sigma v \rangle$.

In Eq. (2.16) $|E|$ is just the amplitude of the electric field

$$|E| = \{(Re E)^2 + (Im E)^2\}^{1/2} \quad (2.17)$$

For efficient simulation one has to obtain **analytic** expressions for $\bar{\nu}$, $\bar{\alpha}$ and $\langle \sigma v \rangle$ as functions of $|E|$. It is also convenient to introduce a dimensionless coordinate $\rho = x/w$ in which case Eq. (2.15) can be rewritten as

$$\frac{\partial^2 E}{\partial \rho^2} + 2i \left(\frac{w}{\delta} \right)^2 E = 0 \quad (2.18)$$

where the skin depth δ is given by

$$\delta = \left(\frac{c}{2\pi\sigma\omega} \right)^{1/2} = \left(\frac{cm\nu_{coll}}{2\pi e^2 n_e \omega} \right)^{1/2}$$

It is assumed that the discharge width $w \ll \delta$ and so one can solve Eq. (2.15) by a perturbation expansion by introducing the small parameter $\Delta = (w/\delta)^2$. The electric field can be expanded as

$$E = E_0 + E_1 + E_2 \dots$$

where the terms are ordered in powers of Δ then Eq. (2.15) gives in various orders

$$\frac{\partial^2 E_0}{\partial \rho^2} = 0 \quad (2.19)$$

$$\frac{\partial^2 E_1}{\partial \rho^2} + 2i\Delta E_0 = 0 \quad (2.20)$$

$$\frac{\partial^2 E_2}{\partial \rho^2} + 2i\Delta E_1 = 0 \quad (2.21)$$

.....etc.

Equation (2.19) predicts a constant value for E_0 which after substitution into (2.20) results in

$$E_1(\rho, t) = -2iE_0 \int_0^\rho d\rho' \int_0^{\rho'} \Delta(\rho'') d\rho'' \quad (2.24)$$

Similarly

$$E_2(\rho, t) = -2i \int_0^\rho d\rho' \int_0^{\rho'} d\rho E_1 \Delta d\rho'' \quad (2.25)$$

etc. The SRL code solves the first order equation given by

$$E(\rho, t) = E_0 \left(1 - 2i \int_0^\rho d\rho' \int_0^{\rho'} \Delta(\rho'', t) d\rho'' \right) \quad (2.26)$$

where Δ is found by solving the following rate equations:

$$\frac{\partial n_e}{\partial t} = \nu n_m n_e - \alpha n_e^2 - \beta n_e + D_a \nabla^2 n_e \quad (2.27)$$

$$\frac{\partial n_m}{\partial t} = \gamma n_e - \frac{n_m}{\tau} + D_m \nabla^2 n_m \quad (2.28)$$

D_a and D_m are the ambipolar and metastable atomic diffusion coefficients respectively. D_m is of the order $1/3v_{th}\bar{\lambda} \sim 10^2 \text{ cm}^2/\text{sec/Torr}$ while D_a may probably be 100 times larger ($D_a \sim 10^4 \text{ cm}^2/\text{sec Torr}$). The constant E_o can be found from the boundary condition on the total current

$$\frac{\partial E}{\partial \rho}\bigg|_{\rho=1} = -\frac{2i\omega I_o}{c^2} = -2iE_o \int_0^1 \Delta(\rho', t) \rho' d\rho'$$

or

$$E_o = \frac{\omega I_o}{c^2} / \int_0^1 \Delta(\rho', t) \rho' d\rho' \quad (2.29)$$

The numerical code results will be presented next. The particular slab geometry analysed is shown in Fig. 2.10. The discharge is assumed to be 2.4 cm wide in the x- direction and long in the z direction. The electric field is applied in the y direction. The origin of the abscissa is located at the center of the discharge i.e. the discharge extends between -1.2 cm to 1.2 cm in the x- direction. The stiff current drive will be discussed first since it was the most stable.

2.5.1 A Stiff Current Case

Figure 2.11 shows the temporal and spatial variation of n_e for the discharge between $0 \leq x \leq 1.2 \text{ cm}$. The discharge is assumed to be symmetric hence $-1.2 \text{ cm} \leq x \leq 0$ will just be the mirror image about the ordinate of the plots shown in Fig. 2.11. Also it was assumed that the total current was 2.4 A/cm and the applied electric field was 400 V/cm and the CO_2 laser mixture was 3/2/1 at a total pressure of 30 Torr. The initial spatial electron density was assumed to be slightly greater than 10^{11} cm^{-3} with a non uniformity of 5% between the centre of the discharge and the edge. The attachment rate for electrons was assumed to be $50 \mu\text{s}$. The spatial variation of the electrons is shown every $5 \mu\text{s}$. The initial spatial profile is labeled 1. The curve labeled 2 is spatial profile $5 \mu\text{s}$ later etc. The electron density increased by 20% in the first $10 \mu\text{s}$ and then decrease by 10% during the next $50 \mu\text{s}$. Also the non uniformity at the end of $45 \mu\text{s}$ increased to about 10%. Figure 2.12 shows the results of the next $45 \mu\text{s}$. The curves in Figure 2.12 are spaced every $10 \mu\text{sec}$. The curve labeled 1 in Fig 2.12 is the same as the curve labeled 10 in Fig. 2.11. The curve labeled 2 shows the spatial variation of n_e $10 \mu\text{s}$ later, etc.

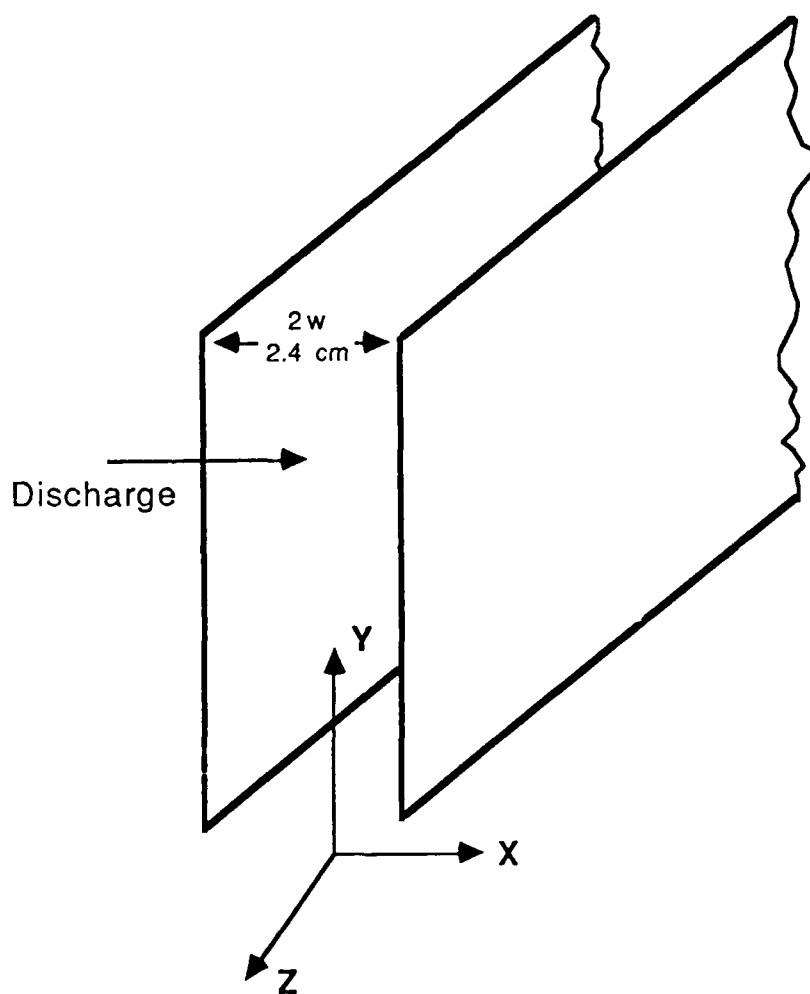


Figure 2.10: Schematic of discharge geometry

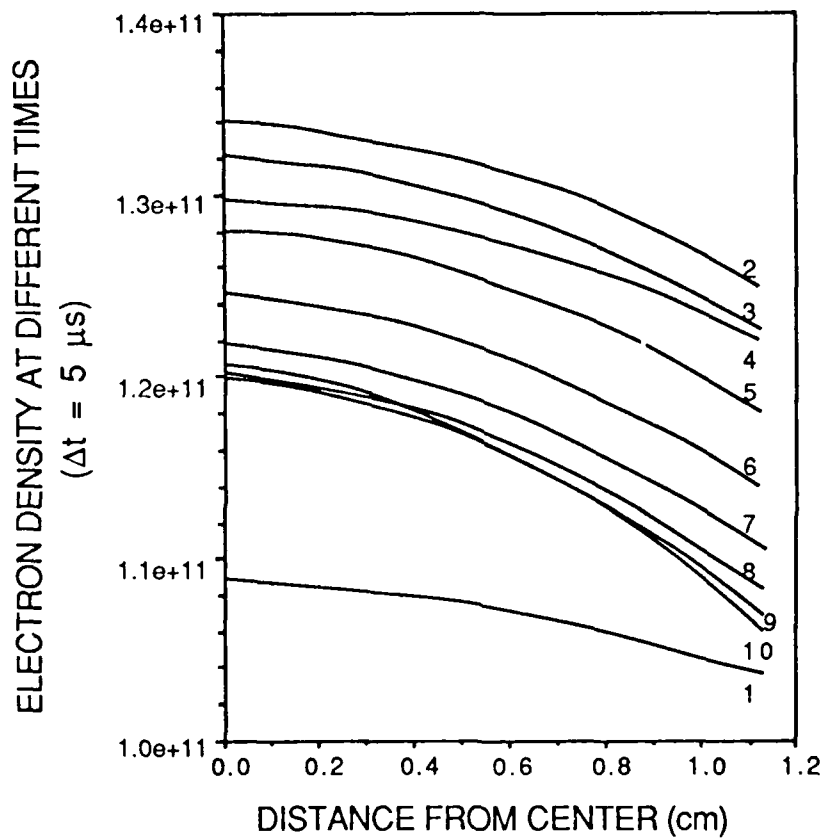


Figure 2.11: Plot showing the spatial and temporal variation of the electron density n_e . Curve 1 is the initial spatial variation of n_e at $t = 0$. Curve 2 is the spatial variation of n_e at $t = 5 \mu s$, etc. The power supply is assumed to be a stiff current source.

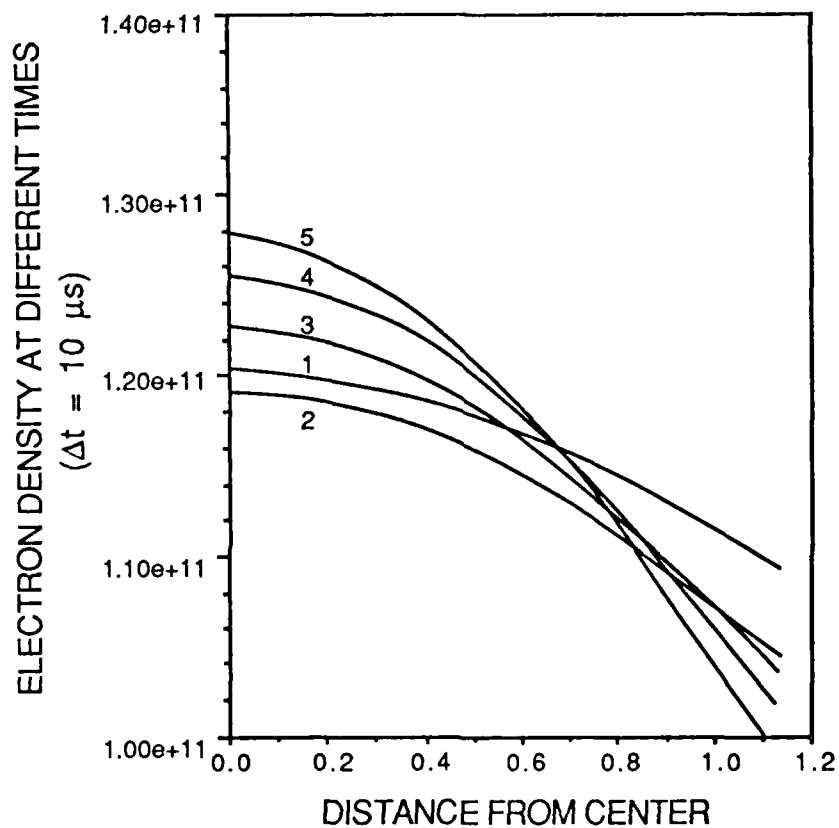


Figure 2.12: The curve labeled 1 is the same as the curve labeled 10 in Figure 2.11. This figure shows the spatial variation of n_e every $10 \mu s$.

The dominant effect is the continual increase in the non uniformity. The uniformity at the end of 85 μs is 25%.

The result shown in Fig. 2.11 and 2.12 show for the conditions assumed the discharge was stable for about 100 μs . However the spatial non-uniformity increases temporally indicating the discharge will eventually be unstable and arcing will occur. From the many code runs analysed it is clear that a spatial non-uniformity and a finite attachment rate results in an unstable discharge even for a stiff current source and the key for stable operation is to obtain as uniform an initial electron density as possible and to keep the electron attachment rate as small as possible.

2.5.2 Stiff Voltage Source

Figures 2.13 and 2.14 show the results of a stiff voltage source for the same conditions discussed previously. In Fig. 2.13 the initial electron density was again chosen to be about $1.1 \times 10^{11} \text{ cm}^{-3}$. The electron density increases by over an order of magnitude in 30 μs . In this figure the spatial variation in the electron density is shown every 3 μs as opposed to every 5 μs in Fig. 2.11 and every 10 μs in Fig. 2.12. This discharge is clearly unstable and it will result in an arc well before the 100 μs pulse length. Figure 2.14 shows the results of initializing the electron density to 10^{10} cm^{-3} . In this case the discharge is clearly quenched. These results are reminiscent of the one dimensional stiff voltage results shown in Figs. 2.8 and 2.9 where discharge is unstable and it proceeds to an arc or its is quenched depending on the initial electron density. So once again it is clear that the stiff current source is more stable than a stiff voltage source.

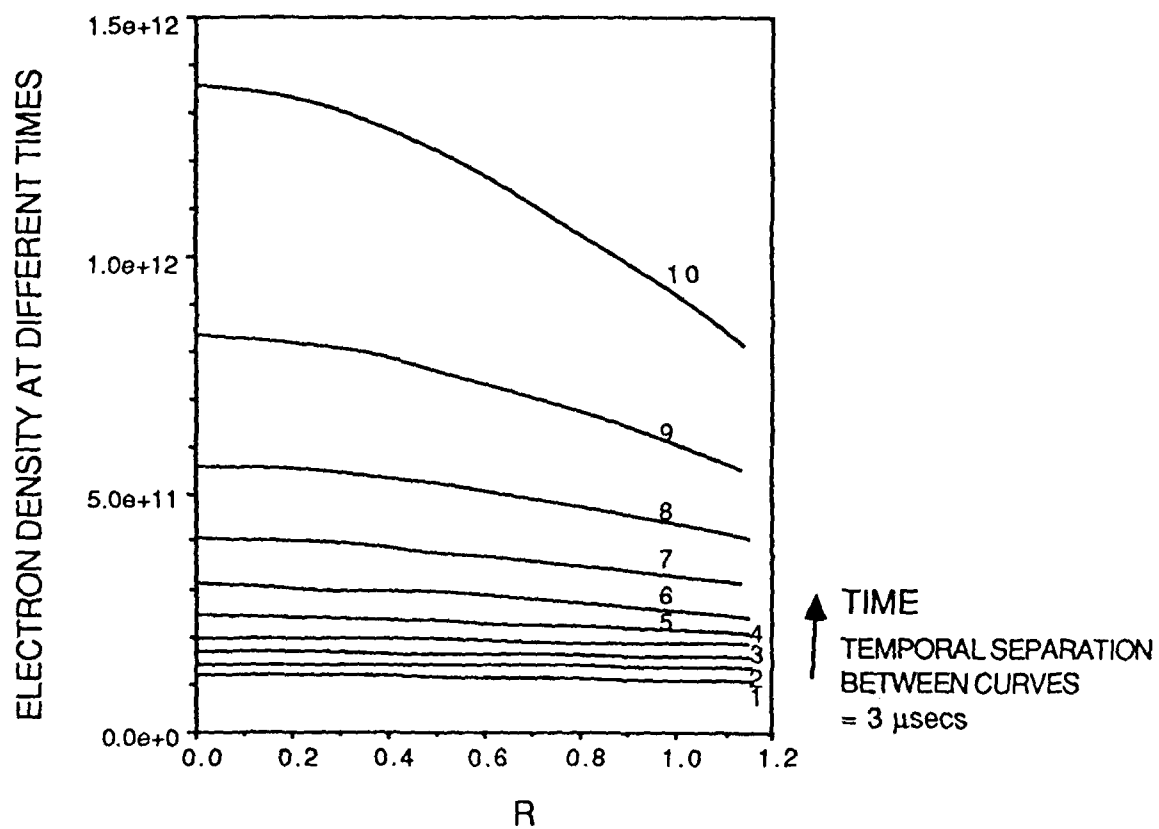


Figure 2.13: Same as Figures 2.11 and 2.12 except that power supply is assumed to be a stiff voltage source and the spatial variation of n_e is shown every $3 \mu\text{s}$.

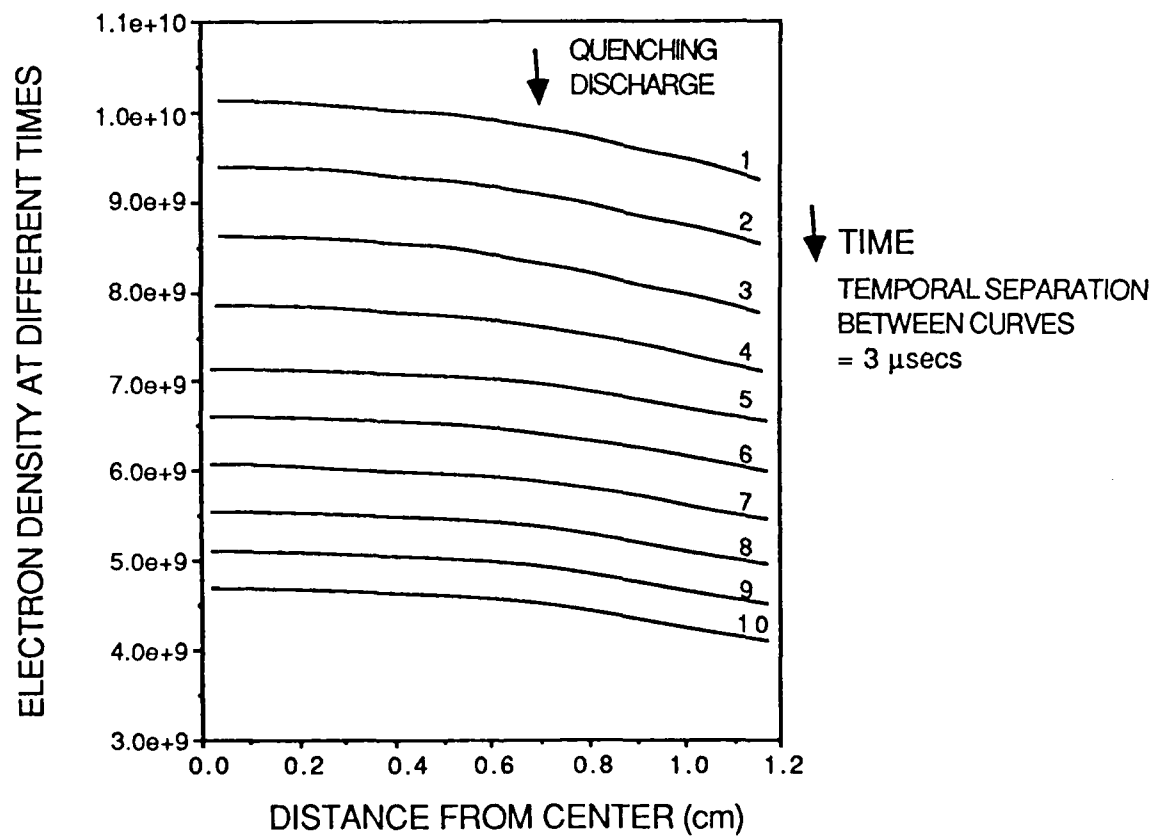


Figure 2.14: Same as Figure 2.13 except that n_e was initialized at 10^{10} cm^{-3}

SECTION 3

3.0 STEADY-STATE CONDUCTION COOLING

In a repetitive pulsed CO₂ laser, the lasing gas must be cooled to prevent thermal population of the lower laser level and a decrease in laser efficiency. At a repetition rate of ν pps, an extraction of W (J/liter), a volume of V (liters) and an electrical efficiency of η , the amount of heat Q which must be carried away from the laser to maintain it at constant temperature is

$$Q = \frac{\nu W V}{\eta} \quad (3.1)$$

For example, for $\nu = 50$ pps, $W = 1.67$ J/liter, $V = 6$ liters and $\eta = 0.167$, values typical of a CO₂ laser operating at a pressure of 30 Torr, one obtains $Q \approx 3.0$ kW. Convecting away this much heat typically requires a flow loop, which increases system weight substantially. In this section the alternative approach of *conduction* cooling will be addressed instead as an advanced concept to minimize the total weight of the laser head. As shown in Fig. 3.1, the heat may be conducted away by the sidewalls along a direction perpendicular to the discharge direction. Conduction cooling is a viable option if the laser is operated at a low pressure and a correspondingly low extraction energy density. Lower extraction energy density and increased laser-head volume result in a lower overall laser head weight when they are linked to the significant weight and volume reductions made possible by the elimination of the flow loop and associated blowers, acoustic damping system and heat exchangers.

3.1 Conduction Equations

For a repetitively pulsed CO₂ laser device the temperature, density and pressure of the lasing gas all vary during each pulse. A repetitively pulsed CO₂ laser applicable to laser radar is expected to have pulses of width ~ 30 μ sec. These pulses are so short that conduction within the laser gas may be ignored during each pulse. The equations coupling the temperature, density and pressure may then be reduced to a third-order equation for the density disturbance driven by the pulsed heating. The finite acoustic speed limits the response of density disturbances of scale sizes greater than ~ 1 cm during each pulse. Between pulses the situation is quite different, however. The pulses are far enough (~ 20 msec) apart for gaseous conduction of the heat to

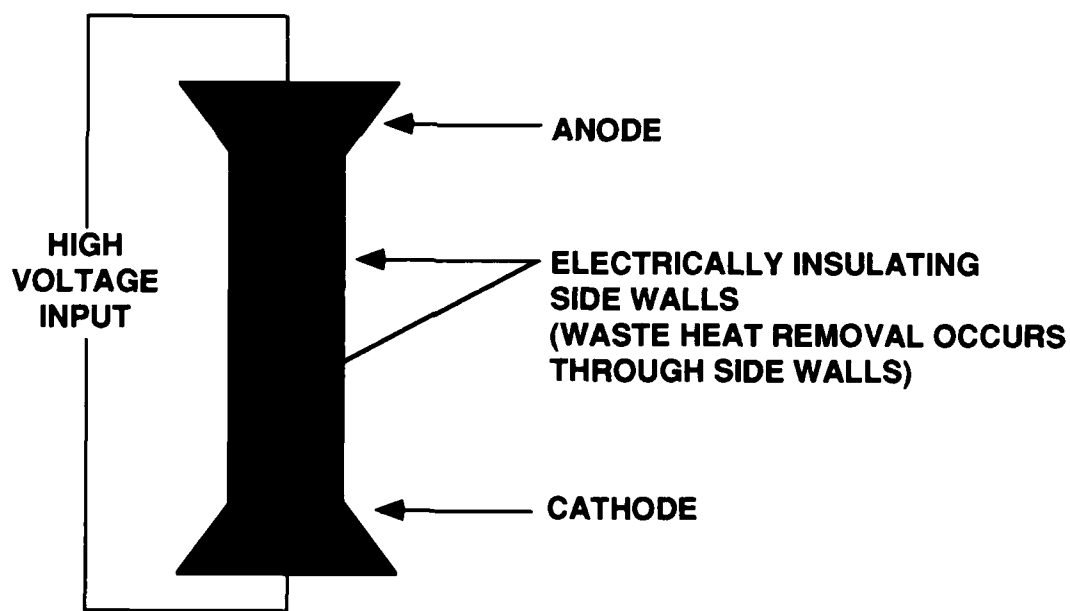
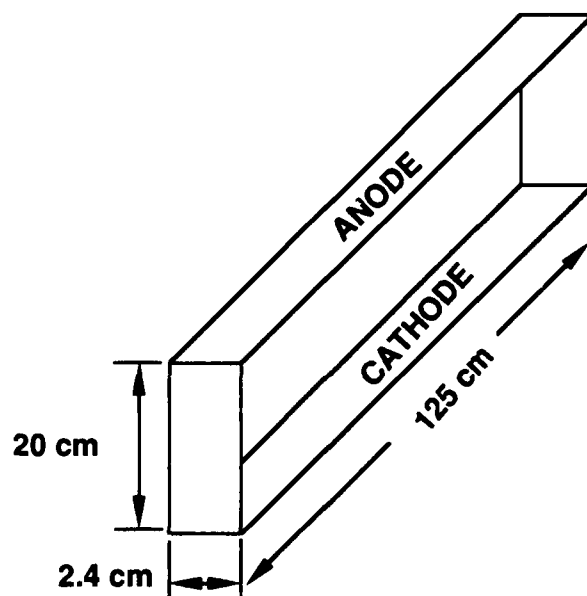


Figure 3.1: Schematic of conduction-cooled CO₂ laser head

64.U190

PROPRIETARY

SCIENCE RESEARCH LABORATORY

be significant. Since the rate of heat conduction is proportional to the temperature gradient, small-scale temperature gradients will tend to conduct away, leaving behind predominantly the largest-scale gradients. After a large number of such pulses, the laser will reach a quasi-steady state, in which the temperature and density are periodic in time with the period of the electrical pumping. In this limit, the effect of each individual electrical pulse on the beam quality is not expected to be severe. However, the cumulative effect of a large number of pulses, balanced against the conduction loss, is expected to lead to steady-state density and temperature profiles which significantly influence the wavefront of the laser beam. This steady-state effect may be calculated approximately by ignoring the pulsed nature of the excitation and treating it as if the heating is uniform in time, with the same average rate as that of the actual repetitively pulsed heating.

For heating which is uniform in time, the equation for the temperature T , including the effect of thermal conduction of the gas, is

$$c_p \frac{\partial T}{\partial t} - \kappa \nabla^2 T = S \quad (3.2)$$

where c_p is the specific heat (at constant pressure) per unit volume, κ is the thermal conductivity of the gas, and S is the heating rate per unit volume. Eq. (3.2) may be written in the alternative form¹

$$\frac{\partial T}{\partial t} - D \nabla^2 T = \frac{S}{c_p} \quad (3.3)$$

where $D = \kappa/c_p$ is the heat diffusivity, which scales as the product of the acoustic speed and the mean-free path between collisions. It is thus inversely proportional to the gas density. Therefore, if the heating source term S/c_p is kept constant as the density is decreased from 1 atm, the effect of heat conduction increases significantly. This may also be seen directly from Eq. (3.2): if one decreases the density and simultaneously decreases S proportionally, then since κ is independent of density the conduction term takes on increasing significance as the density is lowered.

An estimate of the efficacy of conduction cooling for relevant laser conditions may be made directly from Eq. (3.2). Consider a laser channel of dimensions $2.4 \times 20 \text{ cm}^2$, with the surfaces

separated by $d = 2.4$ cm maintained at constant temperature T_0 . For a 3:2:1 He:N₂:CO₂ mix at 400°K, we have $\kappa = 1 \times 10^{-3}$ W/cm °K. In this geometry the cooling is dominated by the effect of the walls spaced 2.4 cm apart. Neglecting the other walls, assuming a spatially uniform heat deposition, and taking the steady-state limit (T independent of time), one may integrate Eq. (3.2) analytically to obtain

$$\Delta T(x) = \frac{W\nu}{2\kappa\eta} x(d-x) \quad (3.4)$$

where x is the distance from one of the walls. At $\nu = 50$ pps, $W = 1.67 \times 10^{-3}$ J/cm³, $\eta = 0.167$, Eq. (3.4) predicts a steady-state temperature rise of ~ 360 K halfway between the walls.

The 1.67 J/liter extraction, 16.7% efficiency and 50 pps repetition rate will be taken to be the baseline parameters of a CO₂ laser amplifier to be used for laser radar. A preliminary analysis indicates that the $d = 2.4$ cm spacing gives adequate conduction cooling at $\nu = 50$ pps; therefore, unless otherwise noted, this spacing will be tentatively considered a baseline parameter, as well. At lower repetition rates, a larger wall spacing can be tolerated.

3.2 Thermal Effect of Pulsed Nature of Heating

One can also solve Eq. (3.2) for the temperature as a function of time, assuming that the energy deposition in the medium is uniform, and that the changes take place at constant pressure. One obtains a maximum temperature rise ΔT_m given by²

$$\Delta T_m = \Delta T_p \left[1 + \left(\frac{4}{\pi} \right) \left(\frac{1}{e^v - 1} - \frac{1}{3(e^{9v} - 1)} + \dots \right) \right] \quad (3.5)$$

In Eq. (3.5) $\Delta T_p = W/c_p\eta$ is the temperature rise due to energy deposition by a single pulse and the dimensionless constant v is given by

$$v = \frac{\kappa}{\nu c_p} \left(\frac{\pi}{d} \right)^2 \quad (3.6)$$

where c_p is the specific heat at constant pressure. For $d = 2.4$ cm, one obtains $v \approx 0.83$, $\Delta T_p \approx 220$ K, and $\Delta T_m \approx 420$ K.

Finally, it is useful to determine the rate at which temperature nonuniformities of different scale sizes are dissipated by thermal conduction between pulses. Let $\delta T_0(x)$ represent the

nonuniform temperature rise at the end of a pulse. Expanding the temperature in Eq. (3.2) in spatial Fourier components yields during the time between pulses

$$c_p \frac{\partial \delta \tilde{T}(k)}{\partial t} + \kappa k^2 \delta \tilde{T}(k) = 0$$

with the solution

$$\delta \tilde{T}(k) = \delta \tilde{T}_0(k) e^{-\kappa k^2 t / c_p}$$

At a repetition rate of ν Hz, the pulses are separated by a time $t = 1/\nu$. Therefore the residual temperature rise of spatial frequency $k_n = \pi n/d$ due to a single previous pulse is given by

$$\frac{\delta \tilde{T}_n}{\delta \tilde{T}_{0n}} = e^{-n^2 v} = \exp\left(\frac{-\kappa \pi^2 n^2}{c_p d^2 \nu}\right)$$

where v is defined in Eq. (3.6), and $n = 1, 2, \dots$ is an integer which characterizes the spatial frequency as a multiple of π/d . As discussed above, $v \approx 0.83$ when $d = 2.4$ cm. Therefore, the temperature component with the *lowest* spatial frequency ($n = 1$) supported by the channel decays by a factor of $\sim \exp(0.83) = 2.3$ between pulses. The component with the next lowest spatial frequency ($n = 2$) decays by a factor of $\sim \exp(6) = 28$ between pulses. Thus the small-scale-size nonuniformities quickly dissipate away between pulses, and to an excellent approximation only the largest-scale temperature nonuniformity needs to be taken into account.

3.3 Scaling of Conduction-Cooled Laser

Eq. (3.4) may be used to scale the laser size as a function of electrical power loading. The steady-state temperature T_c halfway between the walls may be expressed in terms of the electrical power loading $P' = W\nu/\eta$ as

$$T_c - T_0 = \Delta T = \frac{d^2 P'}{8\kappa} \quad (3.7)$$

Thus the temperature rise ΔT is proportional to the power loading and the square of the distance between the walls. This relationship is depicted graphically in Fig. 3.2, which shows the temperature rise as a function of the power loading for various values of channel width (wall separation).

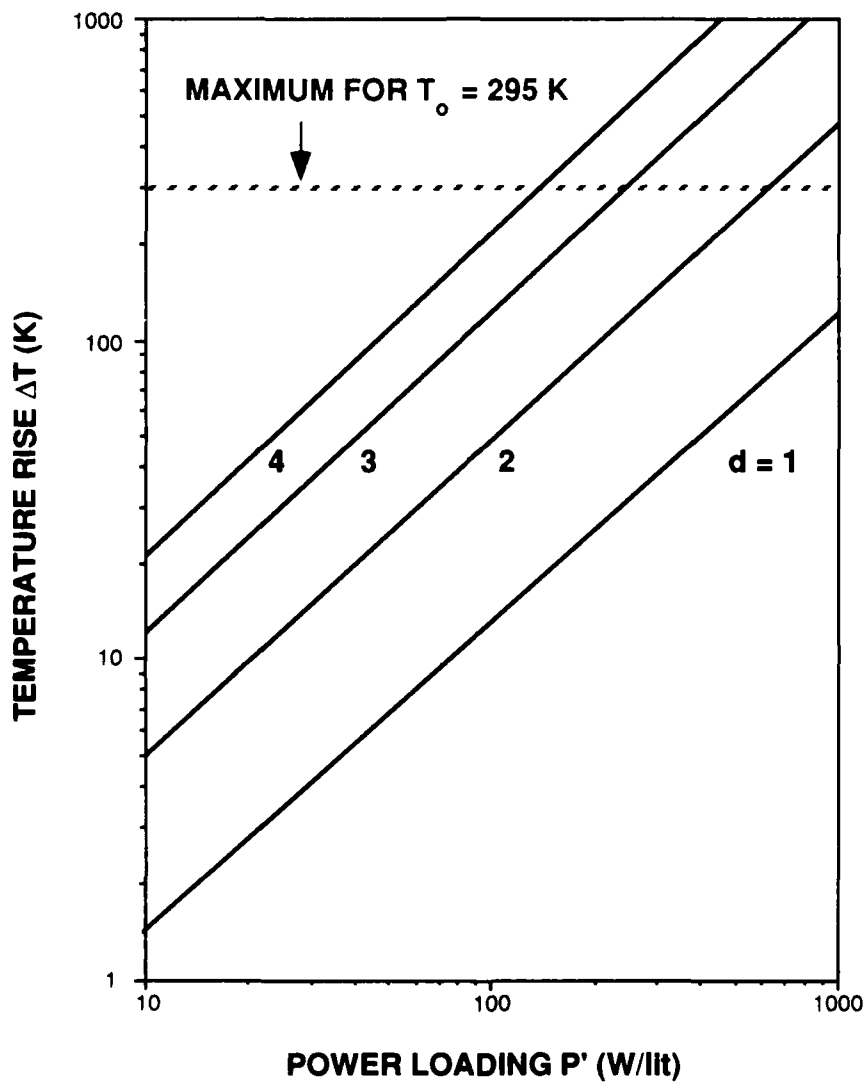


Figure 3.2: Temperature rise versus power loading for various channel widths

The scaling with pulse repetition frequency (PRF) ν may be obtained by rewriting Eq. (3.7) in the form

$$d^2 = \frac{8\kappa}{(W/\eta)} \frac{T_c - T_0}{\nu} \quad (3.8)$$

In Fig. 3.3 the relationship between channel width and PRF is plotted for various values of temperature rise, assuming a single-pulse electrical energy loading W/η of 10 J/lit.

Table 3.1 lists steady-state temperatures and transient temperature rises for a laser head with a 2.4-cm channel spacing operated at various pulse repetition rates (PRF's). At the highest PRF shown (50 pps) it is necessary to maintain the channel walls at a temperature of 200°K (as indicated in Table 3.1) in order to prevent the gas from reaching temperatures at which the lasing efficiency would be degraded. The 200°K temperature is still well above the boiling point (~ 160 -170 K) of CO₂ over the estimated pressure range (30-80 torr) which will apply during operation of the laser.

Table I: Temperature Variation for 2.4-cm-Channel Laser Head

Repetition Rate (Hz)	Steady State Temperature (K)		Transient Temperature Rise (K)	
	At Electrode	At Channel Center	Peak	Beginning of Pulse
10	295	370	210	0
20	295	440	250	30
50	200	560	420	220

3.4 Impact of Conduction Cooling on Beam Quality and Spectral Width in the Steady State

In Section 3.1 it was shown that for a uniform heat deposition, conduction cooling leads to

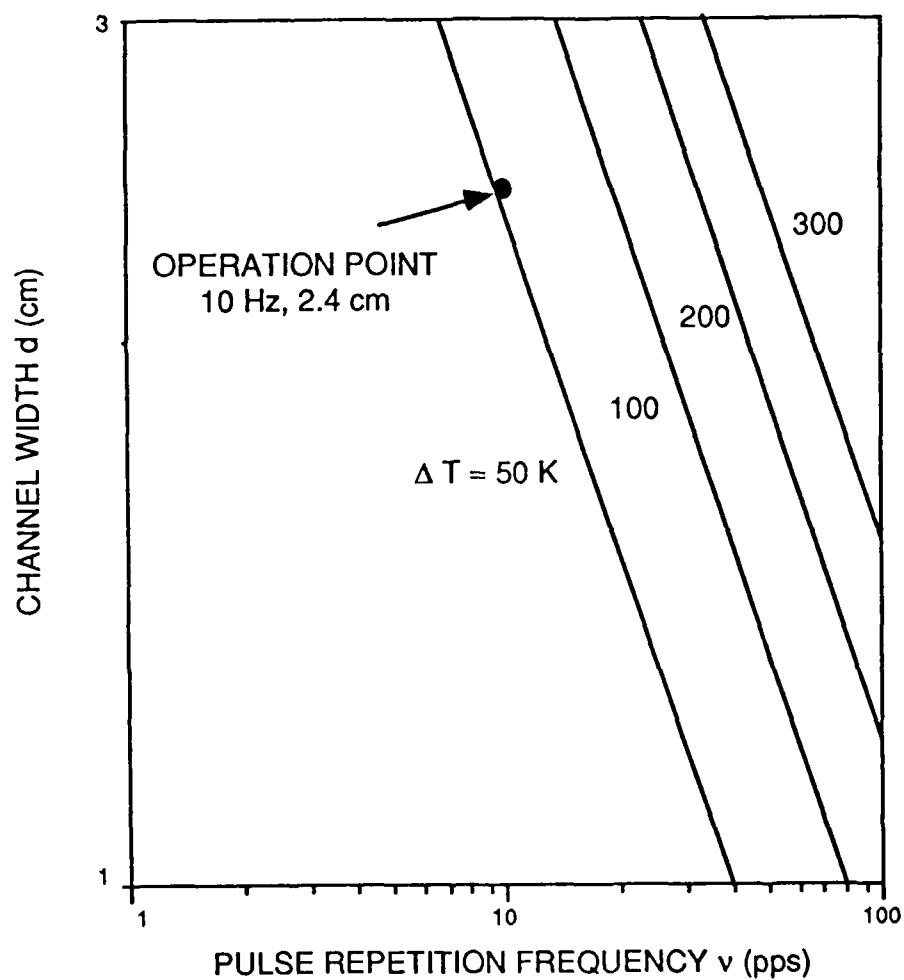


Figure 3.3: Maximum channel width versus PRF for various steady-state temperature rises

a steady state with a quadratic temperature variation across the channel [see Eq. (3.4)]. The quadratic variation of the temperature will, via the equation of state, lead to a corresponding variation in density ρ :

$$\rho = A \left(T_0 + \frac{W\nu x(d-x)}{2\kappa\eta} \right)^{-1} \quad (3.9)$$

where the constant A may be determined from the constraint that the mean value of ρ , averaged over x , must be independent of the heating. The main aberration coming from this density variation will be a negative cylindrical focus along x , i.e., perpendicular to the channel walls.

The associated radius of curvature R may be calculated from

$$\frac{1}{R} = \frac{\lambda}{4\pi} \nabla^2 \phi \quad (3.10)$$

where λ is the wavelength, ϕ is the phase aberration, and $\nabla^2 \phi$ is evaluated at $x = d/2$, halfway between the channel walls. The relationship between phase and density is

$$\phi = \frac{2\pi L_1 \beta_g}{\lambda \rho_A} \quad (3.11)$$

where β_g is the Gladstone-Dale constant (the refractive index minus unity at standard temperature and pressure [STP]) of the laser gas, ρ_A is the gas density at STP, and L_1 is the propagation length. Combining Eqs. (3.9)-(3.11) yields

$$\frac{1}{R} \approx \frac{8 L_1}{3 d^2} \beta_g \frac{\rho_0}{\rho_A} \frac{\mu}{1 + \mu} \quad (3.12)$$

where ρ_0 is the initial density of the gas, and μ is given by

$$\mu = \frac{T_c - T_0}{T_0} = \frac{W\nu d^2}{8\kappa\eta T_0} \quad (3.13)$$

Here T_0 is the wall temperature and T_c is the temperature at the center. The radius of curvature for a single pass through the amplifier ($L_1 = 125$ cm) when $\rho_0/\rho_A = 0.04$ and $\mu = 1$ is

$$R \approx 120 \text{ m}$$

which is reasonably large. For 4 passes through the amplifier, with no correction between passes, the radius of curvature would still be ~ 30 m, corresponding to ~ 0.03 diopters. The cylindrical

focus error can easily be compensated statically by giving the laser beam incident on the laser amplifier a cylindrical focus along x . If the amplifier utilizes an expanding-wave geometry then the optics producing the expansion (perpendicular to x) will be in place, and all that will be needed is a small modification of these optics to produce the relatively small focus along x . Thus, the cylindrical focus, which is the dominant aberration due to the steady-state thermal loading, can easily be compensated and should produce no appreciable beam-quality degradation.

Higher-order aberrations due to the thermal loading may also be present if the electrical heating is not uniform along x . These may be estimated by taking the spatial Fourier transform of Eq. (3.2) in the steady state, yielding

$$T(k) = \frac{S(k)}{\kappa k^2} \quad (3.14)$$

The amplitude of the component of the temperature of spatial frequency k is thus shown to be proportional to the heating nonuniformity of the same spatial frequency and inversely proportional to the square of the spatial frequency. Therefore, as discussed above, small-scale nonuniformities of the steady-state heating do not produce strong temperature and density nonuniformities. The reason is that for a given temperature difference, heat is conducted more rapidly the smaller the scale size of the temperature difference. In the steady state the dominant density disturbance will always be the low-order cylindrical focus, which, as discussed above, is easily compensated. If it turns out to be necessary, it is also possible to compensate some of the higher-order aberrations by utilizing a static adaptive optic which may be adjusted in place to minimize the laser divergence.

It should be noted that the steady-state temperature and density profile distributions have no effect on the spectral purity of the laser. Only the pulsation of the heating, which causes time-dependent changes in the phase, can broaden the spectrum by producing chirp and frequency noise.

A preliminary analysis, sketched above, thus indicates that, as far as the steady state is concerned, conduction cooling to channel walls is a viable technique for carrying away the heat generated in a pulsed CO_2 laser amplifier operated at a low pressure (0.04 atm). The heat generated by each electrical pulse is sufficient to raise the temperature of the laser gas

significantly, on the order of $\sim 300^{\circ}\text{C}$. However, most of this heat conducts away to the walls between pulses. After several laser pulses, a quasi-steady-state temperature and density profile appears. It is comparable with the profile that would obtain if the pulses were replaced by continuous heating at the same rate. The profile is dominated by a quadratic cylindrical focus which, for four passes through the amplifier, is expected to be ~ 0.03 diopters. This negative focus is transverse to the beam-expansion direction, and is easily removed with a slight modification of the focussing optics. It is noteworthy that the negative focus does not appear until the laser amplifier is operated for several pulses so that it reaches its steady-state thermal balance. Higher-order aberrations due to the steady-state heating are predicted to be small, since the temperature gradients which drive them are strongly dissipated by heat conduction. However, it is possible to remove these aberrations, as well, by utilizing a relatively simple static adaptive-optics system. The steady-state heating should have no effect on the spectral purity of the amplified laser beam.

SECTION 4

4.0 ELECTRICALLY GENERATED DENSITY DISTURBANCES

The electrical energy used to pump the laser medium will unavoidably have some degree of spatial nonuniformity. This will result in the generation of acoustical and entropy disturbances, which will in turn produce refractive-index nonuniformities, an increased spectral width, and beam-quality degradation in the laser. Because the channel walls of the discharge-pumped laser are solid, there is no intrinsic spatial discontinuity in the pump-energy distribution, such as that which occurs in an e-beam-pumped laser.³ Still, if the laser medium of interest, discharge-pumped by ~ 10 J/lit in a ~ 30 - μ sec pulse, were used as an oscillator, it would be extremely difficult to maintain the pumping uniform enough to make the oscillator beam quality and spectral quality acceptable. However, as will be shown, the beam-quality degradation and frequency noise are not so severe if the laser medium is used instead as an amplifier. It is expected that the dominant source of the discharge nonuniformities will be nonuniform uv preionization. It is thus possible to make the laser light average over the discharge nonuniformity by ensuring that the uv-preionizing structure changes along the direction of propagation of the laser light. The distance over which this structure must change significantly in order to ensure good beam quality and frequency purity can be determined in detail. In this report, a preliminary estimate of the requirements for good beam quality will be made.

4.1 Density Response to Nonuniform Pumping

The geometry of the laser is shown in Fig. 4.1. The dominant direction of discharge nonuniformity is expected to lie along the direction x transverse to the channel surfaces. Thus, the contributions of nonuniform pumping to density variations along the discharge direction y and the optic axis z may be neglected, and to a good approximation the perturbation ρ of the density satisfies a one-dimensional wave equation of the form⁴

$$\frac{\partial}{\partial t} \left(\frac{\partial^2}{\partial t^2} - u^2 \frac{\partial^2}{\partial x^2} \right) \rho = (\gamma - 1) \frac{\partial^2 Q}{\partial x^2} \quad (4.1)$$

where $Q(x, t)$ is the heating rate, u is the speed of sound, and γ is the ratio of specific heats of the lasing gas. To determine the relevant characteristics of the solutions to these equations one

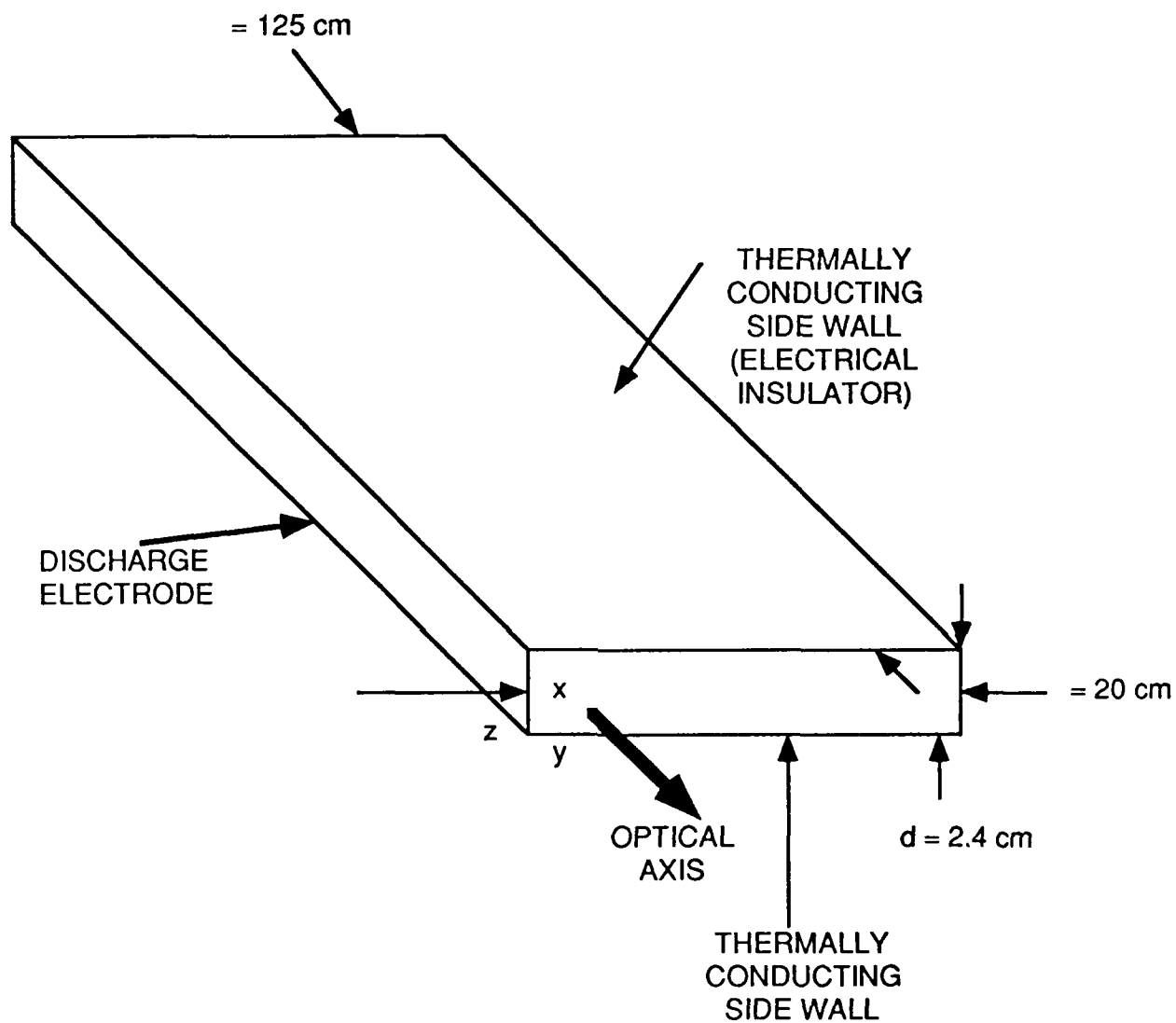


Figure 4.1: Geometry of laser

may impose boundary conditions $\rho = 0$, $Q = 0$ at the walls $x = 0$, $x = d$, which imply that ρ and Q may be expanded in discrete Fourier series as

$$\begin{aligned}\rho(x, t) &= \sum_n \rho_n(t) \sin(k_n x) \\ Q(x, t) &= \sum_n Q_n(t) \sin(k_n x)\end{aligned}\tag{4.2}$$

where $k_n = \pi n/d$ ($n = 1, 2, \dots$) are the allowed spatial frequencies. These are not the most general boundary conditions, but the pertinent characteristics of the solutions will not depend on the boundary conditions except as discussed specifically below.

Substituting Eq. (4.2) into Eq. (4.1) yields

$$\frac{\partial}{\partial t} \left[\frac{\partial^2}{\partial t^2} + (k_n u)^2 \right] \rho_n = -(\gamma - 1) k_n^2 Q_n(t)\tag{4.3}$$

A reasonable approximation is to consider the heating rate to be constant over the interval $0 \leq t \leq \tau$, where τ is the pulsewidth of the electrical pumping. Thus, $Q(x, t)$ may be expressed as $H(x)/\tau$, where $H(x)$ is the total electrical single-pulse energy loading per unit volume. Similarly, $Q_n(t) = H_n/\tau$. The solution of Eq. (4.3) during the pulse is then

$$\rho_n(t) = - \left(\frac{\gamma - 1}{u^2} \right) \bar{H} h_n \left[\frac{u k_n t - \sin(u k_n t)}{u k_n \tau} \right]\tag{4.4}$$

where \bar{H} is the mean energy loading per unit volume, given by

$$\bar{H} = \frac{1}{d} \int_0^d H(x) dx\tag{4.5}$$

and

$$h_n = \frac{2}{d} \int_0^d \left(\frac{H(x)}{\bar{H}} \right) \sin(k_n x) dx\tag{4.6}$$

is the normalized n^{th} Fourier component of the energy loading distribution.

It is useful to consider the form of Eq. (4.4) in the short-time and long-time regimes. $k_n = \pi n/d$ is the frequency of the n^{th} acoustic mode of the channel. For each mode n of wavelength $2\pi/k_n = 2d/n$, one may make the following two observations: (i) When not enough time has passed for a sound wave to have travelled across an acoustic wavelength ($u k_n t < 1$),

$\sin uk_n t \approx uk_n t$ so that $\rho_n \sim t^3$. This is the well-known transient " t^3 " regime of thermal blooming. (ii) For longer times ($uk_n t \gg 1$), corresponding to many acoustic transits across an acoustic wavelength, the blooming reaches the steady state, and ρ_n is instead proportional to t . Thus, the density will respond more strongly to small-scale energy-loading nonuniformities (with $uk_n \tau \gg 1$) than to larger-scale nonuniformities (with $uk_n \tau < 1$).

In the following, spatial averages (over x) will be denoted by $\langle \dots \rangle_x$, and time averages by $\langle \dots \rangle_t$. As will be shown in the next section, the beam quality is determined by the spatial variance of the density perturbation, averaged over the pulse. Using Eq. (4.4), the time-averaged variance may be expanded into its spatial Fourier components, with the result

$$\langle \langle \rho^2 \rangle_x \rangle_t = \frac{1}{2} B^2 \sum_n h_n^2 I_n \quad (4.7)$$

where B , which has the dimensions of a density, is given by

$$B = \left[\frac{(\gamma - 1) \bar{H}}{u^2} \right] \quad (4.8)$$

and $I_n = I(\theta = uk_n \tau)$ is the response function of the n^{th} acoustic mode of the channel to the energy-loading pulse of length τ :

$$I(\theta) = \frac{1}{\theta^3} \left[\frac{\theta^3}{3} - 2 \sin \theta + \frac{1}{2} \theta (1 + \theta \cos \theta) - \frac{1}{4} \sin 2\theta \right] \quad (4.9)$$

The behavior of I as a function of the normalized pulsewidth θ is shown in Fig. 4.2. It is seen that the transition between the short- and long-time regimes is relatively sharp, and that a good approximation for the function $I(\theta)$ is

$$I = \begin{cases} \theta^4/252, & \text{if } \theta < 3; \\ \frac{1}{3}, & \text{if } \theta > 3. \end{cases} \quad (4.10)$$

The t^4 dependence at short times corresponds to the t^6 dependence of ρ^2 implicit in Eq. (4.4), corrected for the fact that at a constant heating rate B^2 would be proportional to t^2 .

4.2 Beam Quality

The energy loading nonuniformity and the density disturbance which it causes will in general not be independent of position z along the optic axis of the laser. In fact, the nonuniformities

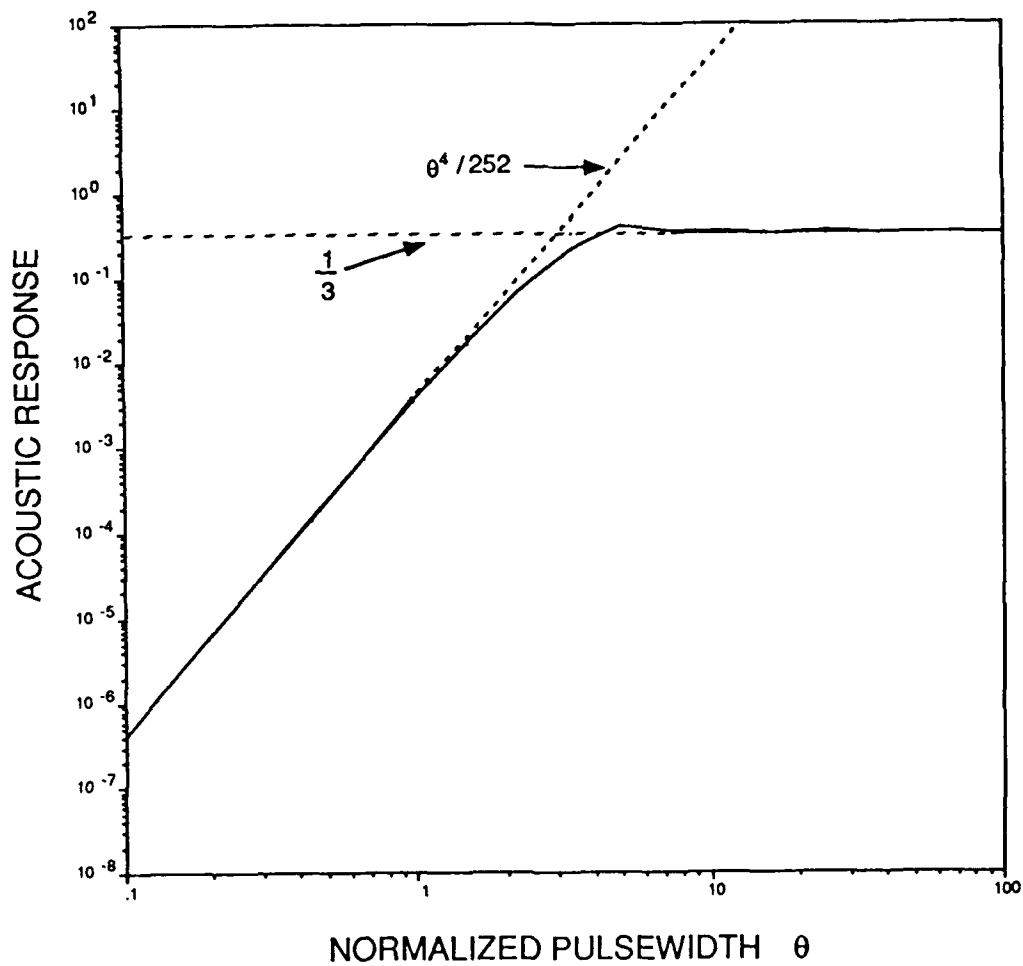


Figure 4.2: Acoustic response versus normalized pulsewidth

will occur in layers along z , with successive layers spatially uncorrelated with each other. The phase aberrations from each layer will therefore add randomly to one another, much like a random walk. The following calculation will concentrate first on the effect of a single layer. The addition of many layers will be carried out subsequently.

The phase aberration $\phi(x, t)$ seen by a ray propagating along z across a single layer is directly proportional to $\rho(x, t)$:

$$\phi(x, t) = \alpha \rho(x, t) = \frac{2\pi L_0}{\lambda} \frac{\beta_g}{\rho_A} \rho(x, t) \quad (4.11)$$

where L_0 is the correlation length along z (i.e., the thickness of the layer), λ is the wavelength of the laser light, β_g is the Gladstone-Dale constant (the difference between the refractive index of the amplifying medium and unity at standard temperature and pressure [STP]), and ρ_A is the density of the amplifying medium at STP. $\phi(x, t)$ may be expanded in a Fourier series of the form

$$\phi(x, t) = \sum_n \phi_n(t) \sin k_n x \quad (4.12)$$

where $\phi_n = \alpha \rho_n$, and the spatial variance of the phase aberration, averaged over time, may similarly be expanded as

$$\langle \phi^2 \rangle_x = \frac{1}{2} \Phi^2 \sum_n h_n^2 I_n \quad (4.13)$$

Here $\Phi = \alpha B$ is given explicitly by the following convenient expression:

$$\Phi = \frac{2\pi L_0}{\lambda} \beta_g \left(\frac{\gamma - 1}{\gamma} \right) \left(\frac{\bar{H}}{p_A} \right) \quad (4.14)$$

where p_A is the standard pressure (1.01×10^5 Nt/m², or, in energy density units, 101 J/lit.) Note that Φ depends only on the energy loading per unit volume and the cell length; in particular, it is independent of pressure. However, at low gas pressures and correspondingly low energy loading, Φ can be reasonably low. A typical value of Φ is 0.31 radians at $L_0 = 5$ cm, $\lambda = 10$ μ m, $\beta_g = 3 \times 10^{-4}$, $\gamma = 1.5$, and $\bar{H} = 10$ J/lit.

Beam quality is determined by the relative value of the peak far-field intensity, known as the Strehl ratio.⁵ In principle, the Strehl ratio depends on both the phase and intensity nonuniformities in the near field. In practice, however, the contribution of the intensity nonuniformity

to deviations of the Strehl ratio from unity is usually negligible. For the case at hand the Strehl ratio $S(t)$ may then be written as

$$S(t) = \left| \langle e^{i\phi(x,t)} \rangle_x \right|^2 \quad (4.15)$$

where, as above, the brackets $\langle \dots \rangle_x$ denote a spatial average over the near-field beam (i.e., over x). Expanding the exponent in powers of ϕ yields

$$S(t) \approx 1 - (\langle \phi^2 \rangle_x - \langle \phi \rangle_x^2) \quad (4.16)$$

to order ϕ^2 . In general, one is interested in the temporal average of the beam quality. Let \tilde{S} be the time average of $S(t)$. It follows from Eq. (4.16) that

$$\tilde{S} \approx 1 - \langle \langle \phi^2 \rangle_x \rangle_t + \langle \langle \phi \rangle_x^2 \rangle_t \quad (4.17)$$

When $|\phi - \langle \phi \rangle| \geq 1$ this approximation breaks down, and higher powers of ϕ must be included. If the energy-loading distribution satisfies Gaussian-normal statistics then the power series may be summed, yielding

$$\tilde{S} \approx \exp \left[- \langle \langle \phi^2 \rangle_x \rangle_t + \langle \langle \phi \rangle_x^2 \rangle_t \right] \quad (4.18)$$

[For other statistical distributions of the energy loading Eq. (4.18) is correct only to order ϕ^2 ; Eq. (4.18) and all subsequent equations describing beam quality should in general be considered to be correct only to this order.]

The presence of hard boundaries confining the gas in a fixed volume forces the mean density, averaged over x , to be a constant, independent of t . Therefore $\langle \phi \rangle_x = 0$. Combining Eqs. (4.10), (4.13), and (4.14), one arrives at the following result:

$$\tilde{S} \approx \exp \left\{ -\frac{1}{2} \Phi^2 \left[\left(\frac{\pi u \tau}{d} \right)^4 \sum_{n < n_0} n^4 h_n^2 + \frac{1}{3} \sum_{n > n_0} h_n^2 \right] \right\} \quad (4.19)$$

where

$$n_0 = \frac{3}{\pi} \frac{d}{u \tau} \quad (4.20)$$

is approximately the number of acoustic transits across the channel during the electrical pulse. By way of example, for $d = 2.4$ cm, $\tau = 30$ μ sec, and $u \approx 400$ m/sec, the value of n_0 is ~ 1.9 .

It should be noted that beam quality is often measured in "number of times diffraction limited" (XDL). The relationship between XDL and \tilde{S} is

$$XDL = \frac{1}{\sqrt{\tilde{S}}} \quad (4.21)$$

so that Eq. (4.19) implies that

$$XDL \approx \exp \left\{ +\frac{1}{4}\Phi^2 \left[\left(\frac{\pi u \tau}{d} \right)^4 \sum_{n < n_0} n^4 h_n^2 + \frac{1}{3} \sum_{n > n_0} h_n^2 \right] \right\} \quad (4.22)$$

The above results apply to the propagation through a single correlation length (along z) of the density disturbance. Since successive layers are spatially uncorrelated, the propagation through several correlation lengths results in the addition of the squares of the phase errors. The generalizations of Eqs. (4.19) and (4.22) are thus

$$\tilde{S} \approx \exp \left\{ -\frac{1}{2}\Phi^2 \frac{L}{L_0} \left[\left(\frac{\pi u \tau}{d} \right)^4 \sum_{n < n_0} n^4 h_n^2 + \frac{1}{3} \sum_{n > n_0} h_n^2 \right] \right\} \quad (4.23)$$

and

$$XDL \approx \exp \left\{ +\frac{1}{4}\Phi^2 \frac{L}{L_0} \left[\left(\frac{\pi u \tau}{d} \right)^4 \sum_{n < n_0} n^4 h_n^2 + \frac{1}{3} \sum_{n > n_0} h_n^2 \right] \right\} \quad (4.24)$$

where L is the total distance travelled by the laser beam through the amplifier, so that L/L_0 is the number of correlation lengths traversed by the laser beam.

It is useful to break the right-hand side of Eq. (4.24) into two parts, as follows:

$$XDL \approx \exp \left\{ +\frac{1}{4}\Phi^2 \frac{L}{L_0} [\delta_L + \delta_S] \right\} \quad (4.25)$$

where δ_L and δ_S are the contributions from large- and small-scale nonuniformities, respectively, in the electrical loading:

$$\begin{aligned} \delta_L &= \left(\frac{\pi u \tau}{d} \right)^4 \sum_{n < n_0} n^4 h_n^2 \\ \delta_S &= \frac{1}{3} \sum_{n > n_0} h_n^2 \end{aligned} \quad (4.26)$$

δ_L is the contribution of transient thermal blooming caused by large-scale nonuniformities (scale size $> u\tau$) in the electrical energy loading. Because of the factor of $(\pi u\tau n/d)^4$ in this term, it is generally small (see Fig. 4.2). On the other hand, δ_S is due to the steady-state thermal blooming caused by small-scale nonuniformities (scale size $< u\tau$) in the energy loading. Because of the relatively strong steady-state response of the medium to the smaller scales, it is δ_S which must be carefully monitored in the design of the laser amplifier.

A useful alternative expression for δ_S is

$$\delta_S \approx \frac{2}{3} \langle h_S^2 \rangle_x = \frac{2}{3} [h_{S,rms}]^2 \quad (4.27)$$

where $h_S(x)$ is the small-scale fractional modulation in the energy loading:

$$h_S(x) = \frac{H(x) - \bar{H}}{\bar{H}} \Big|_S \quad (4.29)$$

Combining Eq. (4.28) with the definition of Φ yields

$$XDL \approx \exp \left\{ +\frac{1}{6} \left(\frac{2\pi}{\lambda} \beta_g \frac{\gamma - 1}{\gamma} \frac{\bar{H}}{p_A} \right)^2 L L_0 [h_{S,rms}]^2 \right\} \quad (4.29)$$

For a given required XDL , Eq. (4.29) may be used to determine the acceptable range of L_0 and rms variation in the energy loading. By way of example, for three passes through a 125-cm amplifier one has $L = 375$ cm. With $\lambda = 10 \mu\text{m}$, $\beta_g = 2 \times 10^{-4}$, $\gamma = 1.5$, and for $\bar{H} = 10$ J/liter, Eq. (4.29) reduces to

$$XDL \approx \exp \left\{ +\frac{L_0 (h_{S,rms})^2}{9} \right\} \quad (4.30)$$

where L_0 is in cm. Eq. (4.31) implies that energy-loading nonuniformities as large as $\sim 20-30\%$ rms are consistent with excellent beam quality (1.1 XDL) if the correlation length is of the order of 10 cm or less.

This preliminary analysis thus indicates that the requirements for little effect on beam quality from the acoustics driven by a single pulse are relatively easy to achieve. It is proposed that a more detailed analysis, including realistic deviations from Gaussian-normal statistics, will be carried out during the course of this program.

4.3 Frequency Noise

A second important effect of the density changes during the pulse is changes in the frequency of the amplified laser light. In general, these frequency changes may be divided into two distinct parts: chirp and frequency "noise." The chirp ν_{ch} is the change in the instantaneous central frequency of the light, while the noise $\delta\nu$ is associated with deviations from the instantaneous central frequency, i.e., creation of Fourier components at other frequencies. For a laser amplifier with solid walls, the chirp should be nearly zero if the laser beam uniformly fills the entire region between the walls (i.e., if the laser intensity is independent of x). Deviations from uniformity may produce some chirp.

4.4 Mode-Medium Instability

Another effect that could in principle prove relevant to controlling the beam quality of a pulsed CO₂ laser is the mode-medium instability (MMI), which has been described in detail in Ref. 4. The MMI is due to the interaction between the laser intensity distribution, the dependence of the heating rate on the laser inversion, the acousto-density response of the gaseous medium to the heating distribution, and the refraction/diffraction of light by the density disturbance.

It is anticipated that a CO₂ laser amplifier of the type used for laser radar will not suffer any significant loss from MMI. As was shown by Flusberg et. al., the instability is important in a laser oscillator,⁴ but does not cause a loss of beam quality in a laser amplifier.^{6,7} In addition, even in an oscillator, the rate at which the instability grows depends on density; at a density of 30-40 torr the degradation in oscillator beam quality should occur on a time scale of ~ 100 μ sec, hence there should be no significant effect on the beam quality of a 30- μ sec pulse.

4.5 Persistent Acoustic Disturbances

Another important effect on beam quality is that of persistent acoustic disturbances, which are created by the heat deposition during each pulse. Between pulses these disturbances relax from the combined effects of viscous damping in the gas and imperfect acoustic reflections from the solid boundaries. For a repetitively pulsed laser, each successive pulse "feeds" the various acoustic modes of the laser cavity. Each mode decays between pulses but is driven again by

successive pulses. The result is a steady state between the driving impulses due to the pulsed heat deposition on the one hand and the damping by viscosity and finite reflectivity on the other. For a small enough wall reflectivity the acoustics should damp away so rapidly that no significant buildup should take place.

References

1. H. Carslaw and J. Jaeger, *Conduction of Heat in Solids, Second Edition*, Clarendon Press, Oxford, 1986.
2. J. Daugherty, "Electron-Beam Ionized Lasers," in *Principles of Lasers Plasmas*, edited by G. Bekefi, Wiley, 1976.
3. E. Pugh, J. Wallace, J. Jacob, D. Northam, and J. Daugherty, "Optical Quality of Pulsed Electron-Beam Sustained Lasers," *Applied Optics* 13, pp. 2512-2517, 1974.
4. A. Flusberg, D. Korff, T. Cronburg, and G. Theophanis, "Mode-Medium Instability in Pulsed CO₂ Lasers," *Proceedings, International Conference on Lasers '83*, STS Press, McLean, Virginia, 1983, pp. 503-511.
5. M. Born and E. Wolf, *Principles of Optics, Fourth Edition*, Pergamon Press, 1970, pp. 460-462.
6. G. Theophanis, A. Flusberg, and R. Litte, "Pulsed Electric Discharge Laser Technology Development Program, EDL Focusability, and Van Test," Avco Everett Research Laboratory Final Technical Report, U.S. Army Missile Command Directed Energy Directorate, 1984.
7. G. Theophanis, A. Flusberg, and D. Korff, "Pulsed Electric Discharge Laser Technology Development Program, Lost Energy Testing," Avco Everett Research Laboratory Final Technical Report, U.S. Army Missile Command Directed Energy Directorate, 1984.